ARTICLES
https://doi.org/10.1038/s41589-019-0225-6
nature chemical biology

# Designing a chemical inhibitor for the AAA protein spastin using active site mutations

Tommaso Cupido[1], Rudolf Pisa[1,2], Megan E. Kelley[1] and Tarun M. Kapoor[1]*

**Spastin is a microtubule-severing AAA (ATPases associated with diverse cellular activities) protein needed for cell division and intracellular vesicle transport. Currently, we lack chemical inhibitors to probe spastin function in such dynamic cellular processes. To design a chemical inhibitor of spastin, we tested selected heterocyclic scaffolds against wild-type protein and constructs with engineered mutations in the nucleotide-binding site that do not substantially disrupt ATPase activity. These data, along with computational docking, guided improvements in compound potency and selectivity and led to spastazoline, a pyrazolyl-pyrrolopyrimidine-based cell-permeable probe for spastin. These studies also identified spastazoline-resistance-conferring point mutations in spastin. Spastazoline, along with the matched inhibitor-sensitive and inhibitor-resistant cell lines we generated, were used in parallel experiments to dissect spastin-specific phenotypes in dividing cells. Together, our findings suggest how chemical probes for AAA proteins, along with inhibitor resistance-conferring mutations, can be designed and used to dissect dynamic cellular processes.**

In humans, the AAA superfamily (ATPases associated with diverse cellular activities) has ~100 proteins whose functions have been linked to a wide range of cellular processes, including cell division, cytoskeleton organization, and organelle biogenesis[1]. As AAA proteins carry out functions that can occur within minutes to seconds, chemical probes that inhibit their activities in cells on similarly fast timescales can be valuable tools to dissect dynamic mechanisms[2]. Currently, we have well-characterized selective chemical probes for only a handful of AAA proteins, such as dynein, a microtubule-based motor protein, midasin, a ribosome biogenesis factor, and valosin-containing protein (VCP), a regulator of ubiquitin-dependent proteolysis[3–6]. However, chemical inhibitors of most AAA proteins are not available.

Spastin, fidgetin, and katanin are AAA proteins closely related at the level of sequence and are collectively referred to as microtubule-severing enzymes[7]. Biochemical assays have shown that spastin and katanin can sever microtubules into smaller filaments in an ATP-hydrolysis-dependent manner[8,9]. On the basis of these findings, models have been proposed for how microtubule-severing enzymes contribute to the assembly, disassembly, or maintenance of microtubule-based structures in axons and dendrites, primary cilia, and dividing cells[10]. In addition, recent studies have suggested a role for spastin in the biogenesis and function of the nuclear envelope and membrane organelles, such as lysosomes and endosomes[11–13]. Thus far, the only chemical proposed to target a microtubule-severing enzyme in cells is a purine-based compound that can pull-down katanin from cellular lysates[14]. However, the direct and specific inhibition of katanin by this compound has not been demonstrated[14], and it is unclear how useful chemical probes for microtubule-severing proteins can be developed.

In principle, chemical inhibitors of AAA proteins can be identified that target either the nucleotide-binding site or an allosteric site. An allosteric inhibitor-binding site has been characterized for VCP and the vacuolar protein sorting-associated protein 4 (VPS4)[15,16]. However, it is unclear whether an equivalent site exists in microtubule-severing other AAA proteins. Targeting the nucleotide-binding site could represent a more general strategy; however, designing selective nucleotide-competitive inhibitors of AAA proteins is challenging for at least three reasons. First, the active site is conserved across the AAA superfamily[17]. Second, this site in AAA proteins can undergo activity-associated conformational transitions that substantially alter its overall shape[18]. Third, we lack structural data for any eukaryotic AAA protein bound to a nucleotide-competitive inhibitor. These data can be crucial for structure-based inhibitor design[19].

It is now emerging that analyses of resistance-conferring mutations can help establish the direct physiological targets of chemical inhibitors[20–22]. When these mutations do not disrupt protein activity, they can also be introduced in cells to systematically examine on-target and off-target activities of chemical inhibitors[22]. On-target inhibitor phenotypes can be identified as those observed in cells expressing the wild-type protein but not in those expressing the allele with the resistance-conferring mutation[22]. For these reasons, resistance-conferring mutations could also be useful during the early steps of inhibitor development when unoptimized compounds (for example, screening hits), without robust models for inhibitor–target interactions or data on off-target effects, need to be evaluated. Thus far, resistance-conferring mutations have been typically identified using genetics-based screens that rely on selection of growth in tractable systems, as has been the case for cytotoxic chemical inhibitors of AAA proteins[5,23]. However, identifying mutations in AAA proteins that do not impair function but confer inhibitor resistance can be challenging.

Here we use protein structure and sequence analyses to design mutant alleles of spastin that retain ATPase activity. Testing selected heterocyclic scaffolds against wild-type protein and constructs with these mutations, along with computational docking, helped design spastazoline, a pyrazolyl-pyrrolopyrimidine-based inhibitor of spastin. In addition, we identified a spastazoline-resistance-conferring point mutation in spastin. Spastazoline-induced phenotypes were examined in cells expressing either wild-type spastin or an allele with a resistance-conferring point mutation.

[1]Laboratory of Chemistry and Cell Biology, The Rockefeller University, New York, NY, USA. [2]Tri-Institutional PhD program in Chemical Biology, The Rockefeller University, New York, NY, USA. *e-mail: kapoor@rockefeller.edu

Together, these studies reveal how spastin-specific cell division phenotypes can be analyzed using chemical probes and cognate resistance-conferring mutations.

## Results

**Mutant alleles of spastin that retain ATPase activity.** To design mutant alleles of spastin, we focused on the nucleotide-binding pocket. We selected *Drosophila melanogaster* spastin (hereafter Dm-spastin), as it is a biochemically well-characterized microtubule-severing enzyme[24]. We first compared the sequences of the AAA domains in Dm-spastin and four related AAA proteins: human fidgetin-like protein 1 (Hs-FIGL1), human pachytene homology-like protein 2 (Hs-PCH2), mouse VCP (Mm-VCP, which has two AAA domains and is identical to the human protein), and *Xenopus laevis* katanin (Xl-katanin) (Supplementary Fig. 1a,b). These proteins were selected as recombinant forms of either their AAA domains or constructs with ATPase activity had been previously reported[25–27]. Using available structural data (Dm-spastin, Hs-FIGL1, and Mm-VCP)[15,24,28] or homology-based models (Hs-PCH2 and Xl-katanin; see Methods for details), we identified residues that were likely to be within ~6 Å of adenine (Fig. 1a,b). These residues are located in five structural motifs of the AAA domain, named the amino (N)-terminal loop (N-loop), the phosphate-binding loop (P-loop), the hinge motif, helix 4, and the sensor-II motif[1] (Supplementary Fig. 1c).

As expected for a conserved active site, most of these residues are invariant across the five AAA proteins examined. However, we noted four amino acid positions—one in the N-loop, one in the P-loop, and two in the sensor-II motif—that have diverged significantly (Fig. 1b). These residues, which we name 'variability hot-spot' residues, contribute in large part to the sequence variation in these nucleotide-binding motifs across the AAA proteins (Supplementary Fig. 1d). Sequence alignment of the five structural motifs of the nucleotide-binding site in 24 AAA domains indicates that these variability hot-spot residues can be identified across this protein superfamily (Supplementary Fig. 1e,f). We hypothesized that a residue at a variability hot-spot position could be replaced with a residue from the equivalent position in a related AAA protein, to obtain an active-site mutant that retains enzymatic activity.

To test this hypothesis, we generated recombinant constructs of wild-type Dm-spastin and Dm-spastin carrying mutations at the variability hot-spot residues, and characterized their steady-state ATP-hydrolysis activity (Fig. 1c–e and Supplementary Fig. 1g,h). In addition to the wild-type protein, five of the six mutant constructs were active (Fig. 1d,e and Supplementary Fig. 1h provide additional enzyme activity parameters). Only one construct, with a mutation at a sensor-II variability hot-spot residue (S689R), yielded an inactive recombinant protein (Fig. 1e). Dm-spastin had a catalytic activity ($k_{cat}$) of ~3 $s^{-1}$ (Fig. 1f). The five active mutants had $k_{cat}$ values within ~1.5-fold of the wild-type protein, ranging from ~2 $s^{-1}$ for the N527T mutant to ~4 $s^{-1}$ for the S689A mutant (Fig. 1f). The ATP concentrations required for half-maximal enzymatic velocity ($K_{1/2}$) were also within a narrow range, from ~0.1 mM (wild type, Q488V, and N527T) to ~0.4 mM (S689A) (Fig. 1g). Together, these data indicate that swapping variability hot-spot residues can yield AAA protein alleles that retain catalytic activity.

**A starting chemical scaffold to design spastin inhibitors.** To find chemical starting points for the design of spastin inhibitors, we examined conserved features of the nucleotide-binding site. We noted a pattern of two hydrogen bonds between the adenine and the backbone of a residue in the N-loop in several AAA proteins (for example, A404 in FIGL1 (PDB: 3D8B); G480 in VCP (PDB: 5FTK); Supplementary Fig. 2a). Therefore, we selected and tested a collection of 33 chemically diverse kinase inhibitors, which are heterocyclic scaffolds that could mimic these hydrogen bonding interactions, against AAA proteins (Supplementary Table 1).

To profile the inhibitory activity and selectivity of these compounds, we generated recombinant forms of Hs-FIGL1, Hs-PCH2, Mm-VCP, and Xl-katanin, and characterized their steady-state ATPase activities (Fig. 2a,b and Supplementary Fig. 2b–f). Consistent with other reports, we found $K_{1/2}$ values for ATP hydrolysis to be in the high micromolar range[3,26,29]. Whereas the $k_{cat}$ varied >50-fold (Mm-VCP: ~0.1 $s^{-1}$; Xl-katanin: ~6 $s^{-1}$; Supplementary Fig. 2d), the $K_{1/2}$ values varied only ~3-fold (Hs-PCH2: ~150 µM; Xl-katanin and Mm-VCP: ~450 µM; Fig. 2b). For these enzymes, the range of $K_{1/2}$ was comparable to what we found for the active Dm-spastin mutants, suggesting that variation in the hot-spot residues can account for differences in how these proteins interact with the nucleotide.

We next tested the selected compounds (10 µM) against Dm-spastin and the other four AAA proteins (Fig. 2c). While most compounds did not show appreciable inhibition of any of these enzymes, we identified two compounds, one with a 4-aminopyrazolylquinazoline core (**1**) and the other with a 3,5-diamino-triazole core (**2**) that inhibited at least one AAA protein by >50% (0.5 mM ATP; Fig. 2d and Supplementary Table 1). Both compounds **1** and **2** substantially inhibited the ATPase activity of Dm-spastin at 10 µM, and compound **1** also inhibited Hs-FIGL1 (Fig. 2c). We prioritized compound **1** for further studies here and will examine compound **2** in subsequent work.

Dose-dependent analysis revealed that compound **1** inhibited Dm-spastin with potency in the micromolar range (Fig. 2e). To examine the structure–activity relationship against AAA proteins, we synthesized and tested compound **1** analogs with modifications of the substituents on the pyrazolylquinazoline core (10 µM; Fig. 2f–h, and Supplementary Table 2 shows additional synthesized analogs). We found that compound **3**, in which a benzyl group replaces the phenylacetonitrile, more potently inhibited the activity of VCP compared with compound **1** (Fig. 2f,g). By contrast, compound **4**, in which an *N*-methylpiperazine replaces the phenylacetonitrile and a phenyl replaces the cyclopropyl in the pyrazole ring, showed increased selectivity for Dm-spastin (Fig. 2f,h). Testing Dm-spastin inhibition by compound **4** across a range of ATP concentrations revealed increases in $K_{1/2}$ at higher compound concentrations, but not substantial changes in $k_{cat}$ (Supplementary Fig. 2g,h), consistent with compound **4** binding to the Dm-spastin nucleotide-binding site. Together, these data suggest that the pyrazolylquinazoline scaffold could provide a useful starting point for developing ATP-competitive inhibitors of spastin.

**A model for how compound 4 binds spastin.** To examine how compound **4** binds spastin, we tested it against Dm-spastin constructs with mutations at the variability hot-spot residues. We found that the mutation in the N-loop (Q488V) reduced the potency of **4** by ~20-fold (Fig. 3a), whereas the mutations in the P-loop reduced potency by ~3-fold (N527C) or >35-fold (N527T) (Fig. 3b). By contrast, mutations in the sensor-II motif led to ~2-fold reduction (T692A) or no substantial difference (S689A) in the potency of this inhibitor (Fig. 3c). These data suggested that the P-loop and N-loop variability hot-spot residues may interact with the inhibitor, and this information could be used to confirm or reject predictions from computational docking solutions.

Next, we used available Dm-spastin structural models to dock compound **4** into the spastin nucleotide-binding site[24]. Spastin structures reported to date do not have nucleotide bound, suggesting that the crystallography models may not match the conformation that binds nucleotide-competitive inhibitors[24,30]. To generate additional spastin conformations, we used molecular dynamics simulations and computationally docked compound **4** in the nucleotide-binding site of each spastin conformer[31] (see Methods for

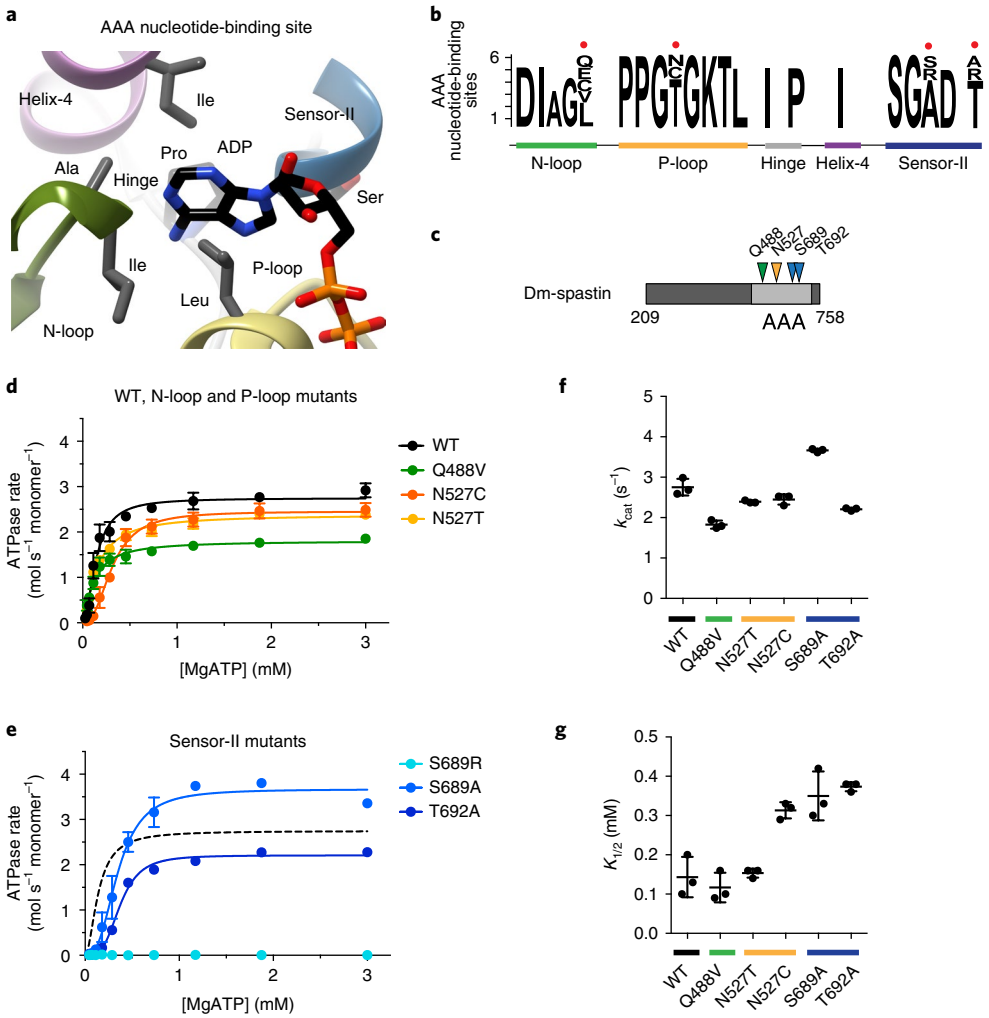


**Fig. 1 | Identifying and characterizing 'variability hot-spot' mutations in spastin. a**, Structural model (ribbon diagram) of the nucleotide-binding site in FIGL1 (PDB: 3D8B) showing adenosine-5′ diphosphate (ADP, stick representation), structural motifs (N-loop, green; P-loop, yellow; helix 4, magenta; sensor-II, blue; hinge, gray), and selected residues within ~6 Å of the adenine. **b**, A modified 'sequence logo' diagram for residues in the nucleotide-binding site of six AAA domains. Four variability hot-spot residues are indicated (red circles). The relevant structural motifs in the nucleotide-binding site are also highlighted. **c**, Schematic shows the AAA domain (light gray box), the first and last residues of the Dm-spastin construct (not to scale), and the residues that were mutated in Dm-spastin's AAA domain (colored arrows). **d**,**e**, ATP-concentration dependence of the steady-state activity of wild-type (WT) and mutant Dm-spastin constructs, analyzed using an NADH-coupled assay. Rates were fit to the Michaelis–Menten equation for cooperative enzymes (average ± s.d., $n = 3$). For comparison, data for the WT protein (from **d**, dashed line) are also shown in **e**. **f**,**g**, Catalytic turnover number ($k_{cat}$; **f**) and the ATP concentration required for half-maximal velocity ($K_{1/2}$; **g**) of recombinant Dm-spastin constructs. Data represent average ± s.d. ($n = 3$). Measured values for these parameters are provided in Supplementary Fig. 1h. The corresponding structural motifs for the mutated residues are color-coded as in **a**.

details). This method yielded four models with similar docking scores for how compound **4** and spastin may interact (Fig. 3d). In three of the four models, we noted adenine-like hydrogen-bonding interactions between the inhibitor aminopyrazole group and the backbone of Dm-spastin N-loop A486 (Supplementary Fig. 3a). However, only two of these docking poses had the inhibitor in close proximity to the variability hot-spot residues in the N-loop and the P-loop and were therefore consistent with the potency shifts observed in the mutant spastin constructs (poses 1 and 2; Fig. 3d and Supplementary Fig. 3a).

We reasoned that the two different docking solutions could arise as a result of the chemical equivalence of the benzene rings in the quinazoline and the pyrazolyl moieties. To distinguish between these two potential binding modes we designed modifications to effectively disrupt the symmetry of the inhibitor. In particular, we synthesized compound **5**, in which the phenyl group in the pyrazolyl was replaced by a non aromatic *tert*-butyl group and the piperazine *N*-methyl group was shifted to the 2-position of the ring (Fig. 3e). Compound **5** inhibited Dm-spastin steady-state ATPase activity (~10-fold more potently than compound **4**; Fig. 3f) and also blocked Dm-spastin-dependent microtubule severing (2 µM inhibitor; Supplementary Fig. 3b–e).

Gratifyingly, docking analysis revealed only one favored pose for compound **5** bound to spastin (Fig. 3g). This model was also consistent with the data obtained by testing mutant constructs (Fig. 3a,c). In this compound **5**–spastin model, the quinazoline core is buried in the adenine-binding pocket within van der Waals distance to the N-loop and P-loop variability hot-spot residues, the piperazine group is proximal to the sensor-II helix, and the aminopyrazole group establishes a network of hydrogen-bonding interactions with the backbone of the N-loop (Fig. 3g and Supplementary Fig. 3f).

**Designing a selective inhibitor of human spastin.** To develop a chemical probe for human spastin, we purified a recombinant form

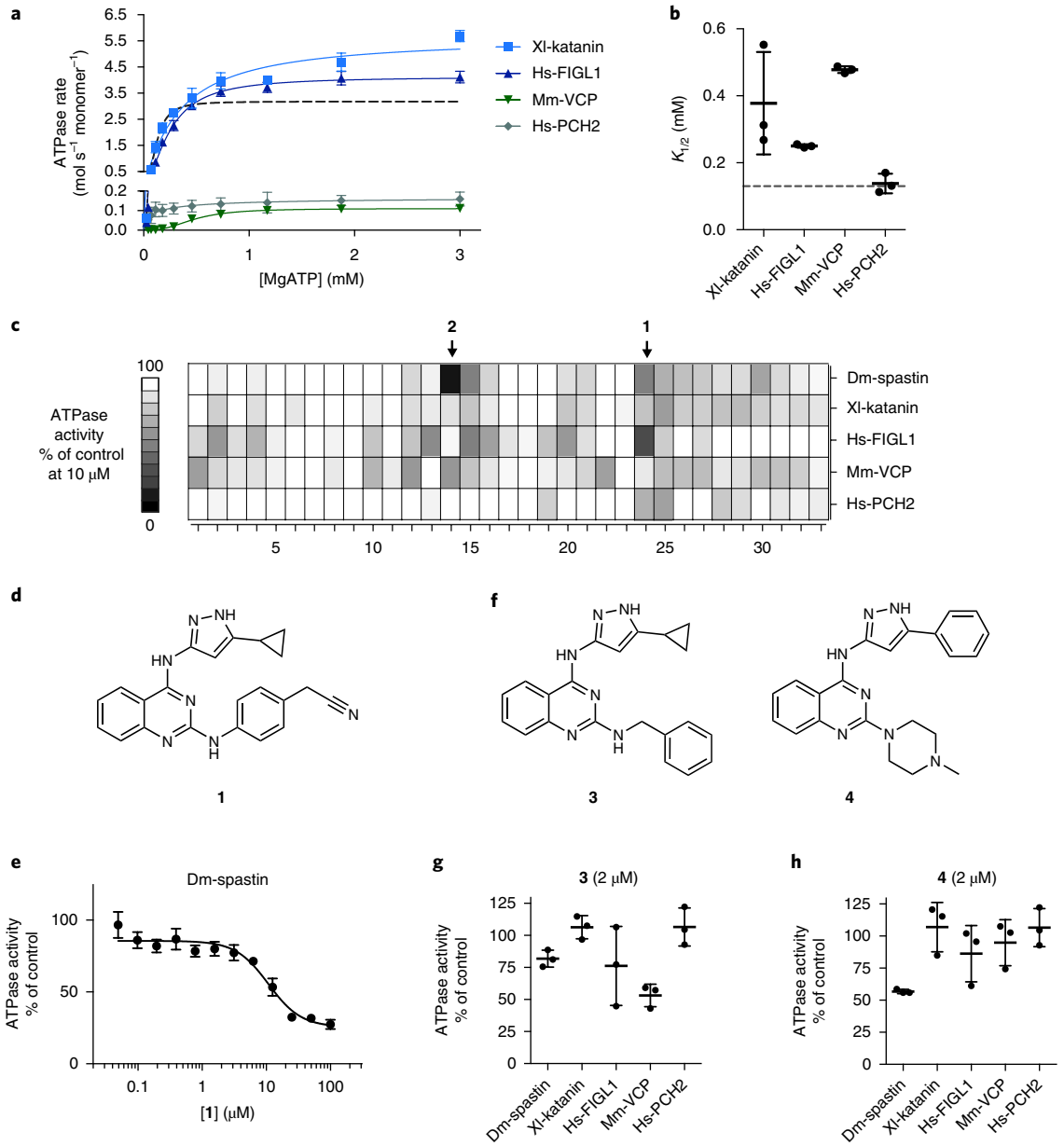


**Fig. 2 | Identifying chemical scaffolds that inhibit Dm-spastin. a**, ATP-concentration dependence of the steady-state activity of four AAA protein constructs, analyzed using an NADH-coupled assay. Schematics for these constructs along with SDS–PAGE gels are shown in Supplementary Fig. 2b,c. Rates were fit to the Michaelis–Menten equation for cooperative enzymes (average ± s.d., $n = 3$). **b**, ATP concentration required for half-maximal velocity ($K_{1/2}$) of four AAA proteins. Data represent average ± s.d. ($n = 3$; for comparison the corresponding data for Dm-spastin are also shown in **a** and **b;** dashed line). Additional enzyme activity parameters are provided in Supplementary Fig. 2d–f. **c**, ATPase activity of five AAA proteins in the presence of selected compounds (10 μM). The heat map corresponds to percentage ATPase activity relative to DMSO control (average, $n = 2$, bins: 10%). Chemical structures of all compounds tested are provided in Supplementary Table 1. **d**, Chemical structure of compound **1** (structure of compound **2** is shown in Supplementary Table 1). **e**, Concentration-dependent inhibition of the steady-state ATPase activity of Dm-spastin by compound **1**. Graph shows percentage residual ATPase activity values relative to DMSO control (average ± s.d., $n = 3$) fit to a sigmoidal dose–response equation; $IC_{50}$ was not determined, as complete inhibition at the highest concentration tested was not observed. **f**, Chemical structures of two analogs of compound **1**. **g**,**h**, Percentage steady-state ATPase activity of five AAA proteins in the presence of compounds **3** or **4** (2 μM). Data represent average ± s.d. ($n = 3$). In the assays in **c**, **e**, **g** and **h**, an MgATP concentration of 0.5 mM was used.

of human spastin (hereafter, Hs-spastin; Supplementary Fig. 4a,b). Hs-spastin had similar ATPase activity relative to Dm-spastin (Supplementary Fig. 4c) and was inhibited by compound **5**, albeit with reduced potency ($IC_{50} = 4.4 \pm 2.1$ μM, 1 mM ATP; average ± s.d., $n = 3$; Fig. 4a).

The inhibitor–Dm-spastin model suggests that the hydrogen at the 8-position of the quinazoline ring of compound **5** would be in close proximity to the N386 side chain in human spastin (equivalent to Dm-spastin N527; Fig. 3g). An asparagine residue is rarely found at the P-loop variability hot-spot position of AAA proteins (Supplementary Table 3). Therefore, we hypothesized that inhibitor potency and selectivity for spastin could be improved by optimizing the interaction with the N386 residue in Hs-spastin. We designed and synthesized an analog in which a pyrrolopyrimidine replaced

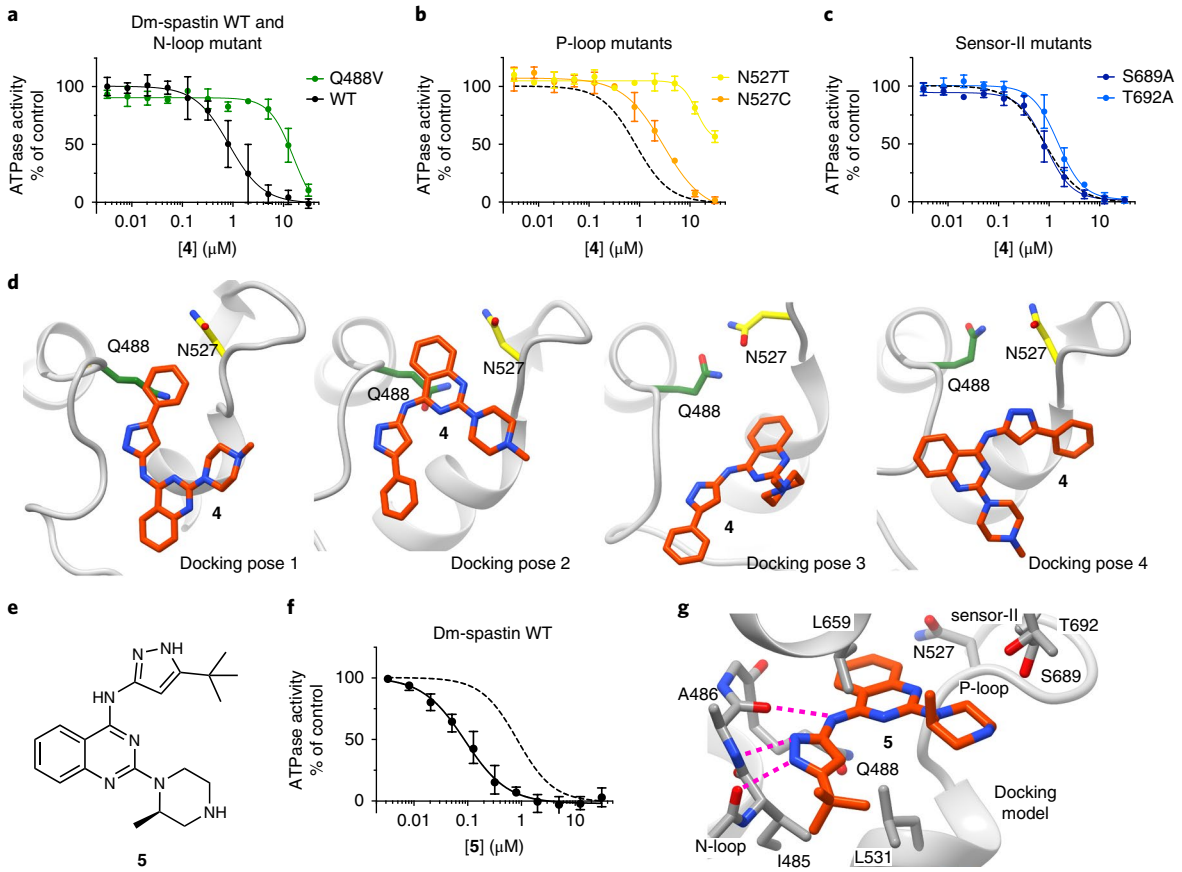


**Fig. 3 | Testing mutant constructs to build a model for the chemical inhibition of spastin. a–c**, Compound **4** concentration-dependent inhibition of the steady-state ATPase activity of Dm-spastin constructs with mutations at variability hot-spot residues and Dm-spastin WT. Data were fit to a sigmoidal dose–response equation and $IC_{50}$ values were calculated (Dm-spastin constructs, WT: 1.0 ± 0.6 μM; Q488V: ~12.5 μM; N527C: 2.9 ± 0.5 μM; N527T: >30 μM; S689A: 0.9 ± 0.2 μM; and T692A: 1.5 ± 0.4 μM; 0.5 mM MgATP, average ± s.d., $n = 3$). For comparison, analysis of the inhibition of WT (data from **a**) is also shown in **b** and **c** (dashed line). **d**, Four computational docking poses showing compound **4** (stick representation, carbon atoms in orange) bound to Dm-spastin (ribbon-and-stick representation, backbone: gray ribbons) along with the Q488 (green) and N527 (yellow) variability hot-spot residues. **e**, Chemical structure of compound **5**. **f**, Compound **5** concentration-dependent inhibition of the steady-state ATPase activity of Dm-spastin WT. Graph shows values fit to a sigmoidal dose–response equation. $IC_{50} = 106 \pm 35$ nM; 0.5 mM MgATP; data show average ± s.d., $n = 3$. For comparison, data for compound **4** are shown (from **a**, dashed line). **g**, Computational docking model for compound **5** bound to Dm-spastin. Potential hydrogen-bonding interactions between the aminopyrazole and the protein backbone are highlighted (dashed lines). Other key amino acids in Dm-spastin nucleotide-binding site are also shown. All images were generated using UCSF Chimera. Additional details of the models are provided in Supplementary Fig. 3a,f.

the quinazoline core of compound **5**, as this would introduce an electropositive group in the position predicted to be proximal to the N386 side chain (compound **6**; Fig. 4b,c). We found that compound **6** inhibited Hs-spastin with ~30-fold improved potency with respect to compound **5** (Fig. 4a; $IC_{50} = 132 \pm 55$ nM, 1 mM ATP; average ± s.d., $n = 3$). Computational docking analysis suggested two possible poses for compound **6** bound to spastin; however, a hydrogen-bonding interaction with the P-loop asparagine was possible in only one pose (Supplementary Fig. 4d).

As kinases are known targets of these chemical scaffolds[32], we examined the activity of compound **6** against 64 human kinases. We found that compound **6** inhibited only four of the 65 kinases by >50% at ~15-fold the $IC_{50}$ for Hs-spastin (2 μM, Supplementary Table 4). To reduce off-target activity, we compared the binding modes of compound **6** to spastin and to kinases using available structural for data inhibitor-kinase interaction. We observed that the piperazine ring of compound **6** is likely to be buried in the interior of the kinase pocket but is facing the bulk solvent in our inhibitor–spastin model (Supplementary Fig. 4e,f). Therefore, we synthesized compound **7** (Fig. 4c), hereafter named spastazoline, in which the 2-methyl in the piperazine group was modified to a 3-isopropyl group so as to increase steric hindrance when interacting with the kinase pocket without disrupting spastin binding. We found that spastazoline only inhibited one of the 65 kinases tested (NTRK1) by >50% (Supplementary Table 4). Importantly, spastazoline potently inhibited Hs-spastin (Fig. 4a; $IC_{50} = 99 \pm 18$ nM; average ± s.d.; $n = 3$, 1 mM ATP) and did not appreciably inhibit any of the four related AAA proteins that we have characterized (10 μM; Fig. 4d). Together, these data suggest that spastazoline could be a useful chemical probe for human spastin if potential off-target effects can be systematically addressed.

We hypothesized that a mutation at N386 would disrupt the spastin–inhibitor interaction and confer resistance to spastazoline. We purified a recombinant Hs-spastin construct with a N386C mutation (equivalent to the N527C mutation in Dm-spastin) and found that the ATPase activity of this mutant construct was comparable to that of wild-type Hs-spastin (Supplementary Fig. 4a–c). As predicted by our model, spastazoline inhibited Hs-spastin-N386C >100-fold less potently than the wild-type protein (Fig. 4e). Additionally, we found that spastazoline did not appreciably stabilize the Hs-spastin-N386C mutant against thermal-induced denaturation ($\Delta T_m$: ~1.5 °C at 200 μM; Fig. 4f and Supplementary Fig. 4g), whereas it considerably

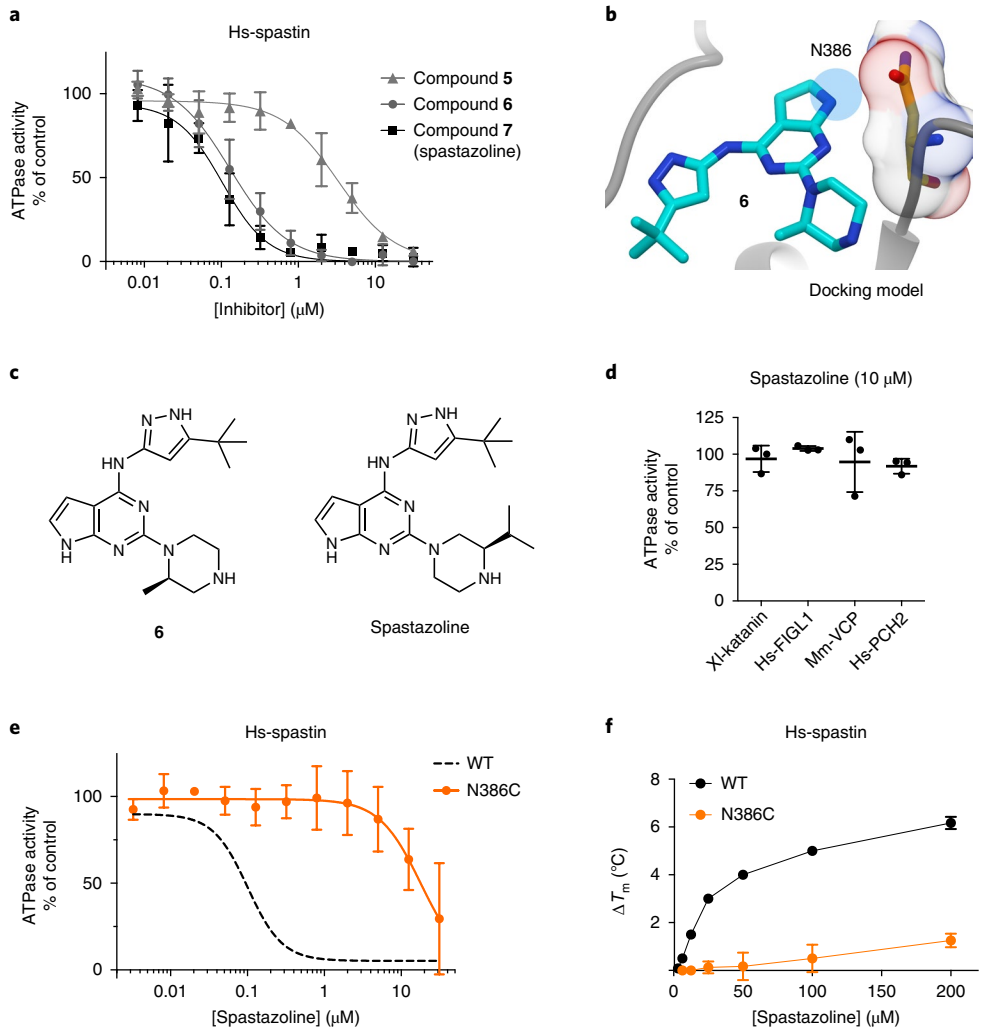


**Fig. 4 | Developing a potent and selective inhibitor of human spastin. a**, Concentration-dependent inhibition of the steady-state ATPase activity of the Hs-spastin construct by compounds **5**, **6**, and **7** (spastazoline). Graph shows values fit to a sigmoidal dose–response equation (average ± s.d., $n = 3$, 1 mM MgATP). $IC_{50}$ values (average ± s.d.; $n = 3$): for compound **5**: 4.4 ± 2.1 μM; compound **6**: 132 ± 55 nM; spastazoline: 99 ± 18 nM. **b**, The predicted model for compound **6** (cyan and blue, stick representation) bound to spastin (gray, ribbon representation) is shown. The N386 residue (stick and surface representation) and the region occupied by inhibitor atoms in close proximity to the N386 residue are also highlighted (blue circle). Additional details of the model are shown in Supplementary Fig. 4d. **c**, Chemical structures of compound **6** spastazoline. **d**, Percentage steady-state ATPase activity of four AAA proteins in the presence of spastazoline (10 μM, 0.5 mM MgATP; data represent average ± s.d., $n = 3$). **e**, Concentration-dependent inhibition of the steady-state ATPase activity of an Hs-spastin mutant construct (N386C). Graph shows values fit to a sigmoidal dose–response equation (average ± s.d., $n = 3$; 1 mM MgATP). For comparison, the curve corresponding to the data for the wild-type Hs-spastin is shown (WT, dashed line; data from **a**). Characterization of the Hs-spastin WT and N386C constructs is shown in Supplementary Fig. 4a–c. **f**, Concentration-dependent effect of spastazoline on the heat-induced unfolding ($\Delta T_m$) of Hs-spastin WT and N386C mutant constructs analyzed used differential scanning fluorimetry (average ± s.d., $n = 3$). Supplementary Fig. 4g,h shows representative differential scanning fluorimetry experiments.

stabilized the wild-type construct ($\Delta T_m$: ~6.0 °C; Fig. 4f and Supplementary Fig. 4h). Together, these data indicate that our approach not only led to a potent chemical inhibitor of spastin, but could also identify resistance-conferring mutations.

**Probing spastin function during cell division.** To probe spastin cellular functions using spastazoline, we focused on the M87e4 spastin (containing the alternatively spliced exon 4), the most abundant spastin isoform in human cells[33] (Supplementary Fig. 5a). As the N386C mutation suppresses spastazoline binding in biochemical assays, we generated two HeLa cell lines in which green fluorescent protein (GFP)-tagged spastin M87e4, either the wild-type (HeLa-WT) or mutant allele (HeLa-N386C), were introduced using the Flp-In T-REx system. We found that these transgenes were expressed at comparable levels (Supplementary Fig. 5a–c).

To examine spastin-dependent inhibitor-induced phenotypes, we focused on cell division. RNAi-mediated spastin knockdown has been shown to disrupt disassembly of the intercellular bridge, a membrane- and microtubule-based structure that connects daughter cells during the final stage of cell division[34] (Fig. 5a). To readily identify intercellular bridges, which are enriched in tubulin post-translational modifications associated with stable microtubules, we imaged acetylated tubulin using immunofluorescence microscopy (Fig. 5b). Treating HeLa-WT cells with spastazoline for 4.5 h (10 μM) resulted in a ~2-fold increase in the number of cells with intercellular bridges compared with DMSO control (25.2 ± 1.4% versus 13.9 ± 0.6%; $n = 3$, average ± s.d.; Fig. 5c and Supplementary Fig. 5d). Importantly, in HeLa-N386C treated with spastazoline, the number of cells with an intercellular bridge was similar to that observed in the DMSO control (13.6 ± 1.4% versus

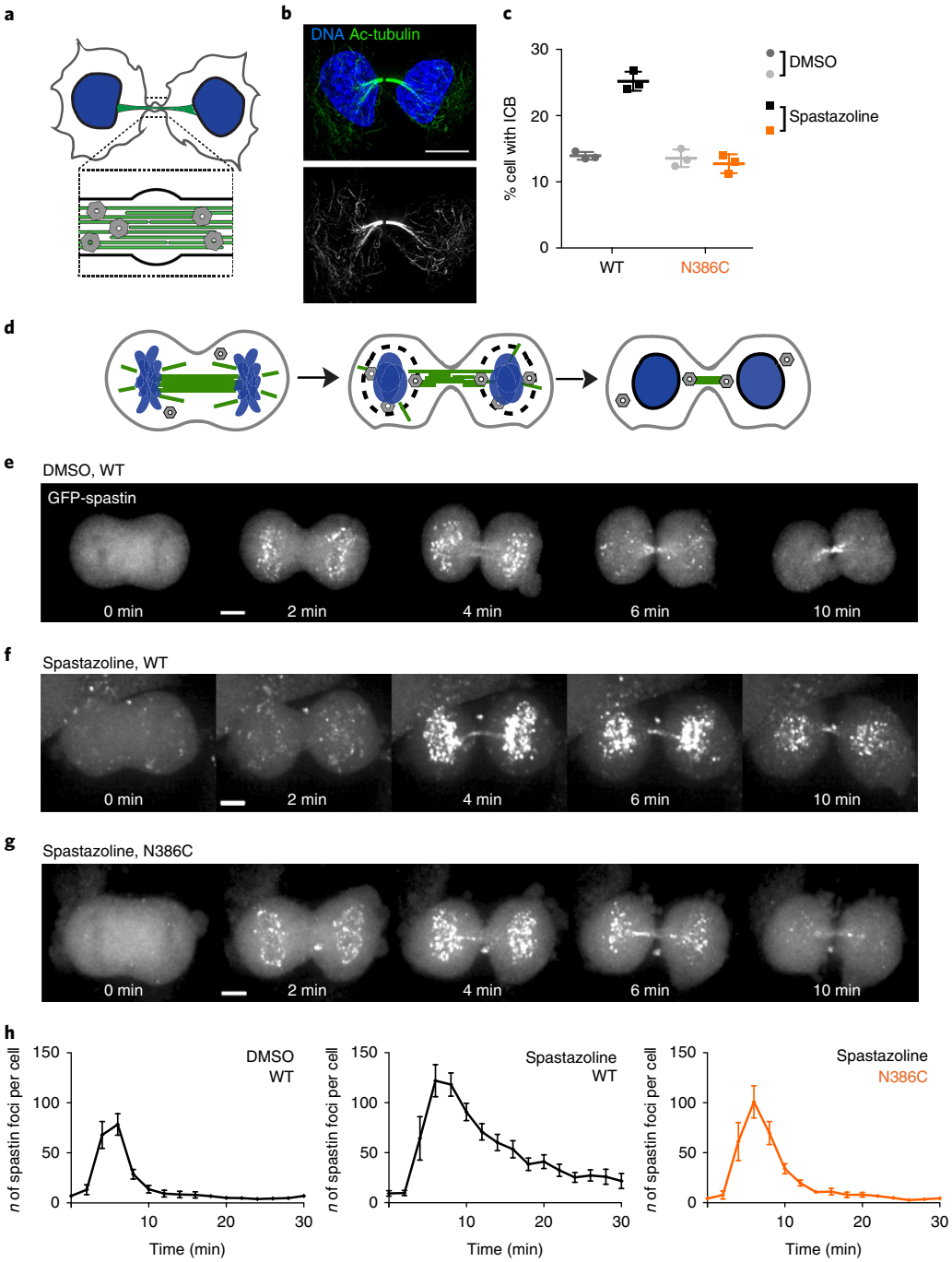


**Fig. 5 | Using spastazoline and a cognate resistance-conferring mutation to probe spastin function in cell division. a**, Schematic for an intercellular bridge (DNA, blue; microtubules, green; spastin, gray). **b**, Immunofluorescence images of fixed HeLa-WT cells stained for acetylated tubulin. Two-color overlay (DNA, blue; acetylated tubulin, green), along with the corresponding grayscale image of acetylated tubulin staining, are shown. Scale bar, 10 µm. **c**, Percentage of cells with an intercellular bridge observed in fixed HeLa-WT and N386C cells treated with DMSO (0.1%) or spastazoline (10 µM) for 4.5 h (data represent average ± s.d., $n = 3$; >2,500 cells analyzed per condition). Representative images for fixed HeLa-WT and HeLa-N386C cells treated with spastazoline and stained for acetylated tubulin are shown in Supplementary Fig. 5d,e. **d**, Schematic of nuclear envelope reformation in a dividing cell, highlighting spastin (gray) localization at the intersection points between microtubules (green), and the reassembling nuclear envelope (black) around chromosomes (blue). **e**–**g**, Effect of spastazoline treatment on spastin localization in dividing cells. Maximum-intensity confocal projections show distributions of GFP at the indicated times after ingression of the cleavage furrow is first observed ($t = 0$) in HeLa-WT cells treated with DMSO control (**e**) and HeLa-WT or N386C cells treated with spastazoline (10 µM for 1 h, **f** and **g**). Scale bars, 5 µm. Representative images from three independent experiments are shown. **h**, Number of spastin foci observed in anaphase HeLa-WT cells treated with DMSO, and HeLa-WT or N386 cells treated with spastazoline ($n = 8$ cells per condition, average ± s.e.m., three independent experiments; values for HeLa N386C cells treated with DMSO are shown in Supplementary Fig. 5j).

12.7 ± 1.3%, $n = 3$; average ± s.d.; Fig. 5c and Supplementary Fig. 5e). Spastazoline treatment (10 µM) did not impact the viability of HeLa cells (Supplementary Fig. 5f) and also did not result in overt changes in the organization of microtubules (Supplementary Fig. 5g). Furthermore, spastazoline did not inhibit ATPase activity of a recombinant human VPS4 (Supplementary Fig. 5h,i), another

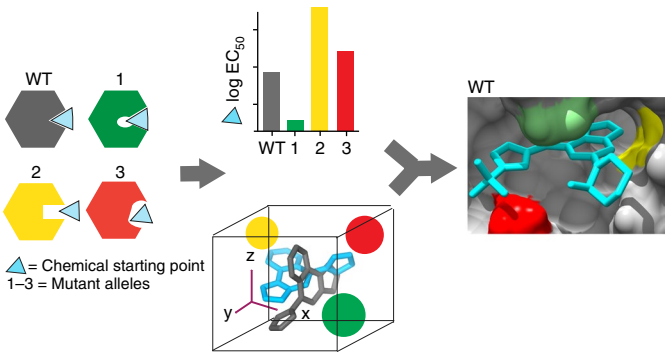


**Fig. 6 | Engineering 'silent' mutations to generate models for inhibitor–target interactions and to identify inhibitor resistance-conferring mutations.** For a selected site in a target protein, constructs with mutations that retain activity are generated to alter its shape and electrostatics. Potency of a chemical scaffold is tested against wild-type and mutant constructs. These data, along with computational docking, can guide improvements in inhibitor potency and specificity and help identify inhibitor resistance-conferring mutations.

AAA protein required for intercellular bridge disassembly[35]. Together, these data indicate that spastazoline inhibits intercellular bridge disassembly by interfering with spastin activity, as the inhibitor-dependent phenotype was observed in wild-type cells but not in cells expressing the inhibitor resistance-conferring allele of spastin.

During anaphase the nuclear envelope is rapidly, within minutes, reformed around daughter nuclei[36] (Fig. 5d). RNAi knockdown studies have revealed a role for spastin in nuclear envelope reformation[13]. To examine the effects of spastazoline during nuclear envelope reformation, we tracked GFP–spastin dynamics in dividing HeLa-WT cells. We found that GFP–spastin accumulated at chromatin within 2–4 min after cleavage furrow ingression initiation (Fig. 5e,h). This signal was lost within ~10 min. These localization dynamics suggest that spastin dissociates as the nuclear envelope reassembles.

Imaging HeLa-WT cells in anaphase treated with spastazoline (10 μM for 1 h) also revealed GFP–spastin puncta on chromosomes (Fig. 5f). Remarkably, spastin puncta persisted for several minutes compared with DMSO controls (Fig. 5f,h). Even 20 min after the initiation of cleavage furrow ingression, the spastazoline-treated cells had a higher number of GFP–spastin puncta than the controls (44 ± 9 versus 5 ± 2, respectively; average ±s.e.m.; Fig. 5h). Imaging HeLa-N386C cells, which express spastazoline-resistant spastin, revealed the recruitment of mutant spastin to anaphase chromosomes with similar kinetics to that of wild-type cells (Supplementary Fig. 5j). However, treatment with spastazoline did not substantially alter spastin dynamics in anaphase HeLa-N386C cells (Fig. 5g). In particular, the number of observed GFP–spastin dots 20 min after cleavage furrow ingression was comparable to that of controls (8 ± 3; 1.6-fold increase with respect to wild type, average ±s.e.m., Fig. 5g,h). Together, these data are consistent with a model in which spastin activity and localization dynamics contribute to nuclear envelope reformation during anaphase.

## Discussion

Here we report the design of spastazoline, an ATP-competitive chemical inhibitor of human spastin. We also identify a cognate resistance-conferring mutation in human spastin that, together with spastazoline, can be used to probe spastin's function in dynamic cellular processes.

Current models indicate that spastin and the endosomal sorting complex required for transport (ESCRT)-III, to which spastin binds[37], coordinate microtubule disassembly with membrane constriction and fusion events during nuclear envelope reformation[13,38]. Our data suggest that inhibition of spastin activity probably suppresses microtubule severing and thereby impairs spastin dissociation and the loss of ESCRT-III from the sites of membrane constriction. RNAi-based knockdown of VPS4 or the ESCRT-III protein, CHMP2A, results in DNA damage associated with compromised nuclear envelope integrity[13]. Consistent with these observations, we suggest that disrupting spastin activity could also result in DNA damage due to defects in nuclear envelope reformation.

Cells depleted of spastin also show defects in the assembly, maintenance, and dynamics of intracellular membrane organelles such as endosomes and lysosomes[11,12]. As the effects of chronic spastin depletion probably accumulate over several hours, the ability to control spastin activity on much faster timescales with spastazoline would be useful to examine intracellular trafficking of membrane organelles. Mutations in the spastin gene are linked to inherited neurodegenerative conditions called hereditary spastic paraplegias[39], and targeting spastin has been proposed as a therapeutic strategy for Alzheimer's disease[40]. In post-mitotic neurons, DNA damage associated with spastin inhibition is not likely, and therefore pharmacological inhibition of spastin in models for neurodegenerative diseases should be further explored. Spastazoline is also likely to be a valuable tool for these studies.

A critical step in our inhibitor-design approach is identifying amino acids in the target protein that can be mutated to alter the shape and electrostatics of the inhibitor-binding site, without substantially disrupting the protein's activity (Fig. 6). In the case of spastin, we find that variability hot-spot residues in the nucleotide-binding pocket can be swapped to introduce mutations to generate alleles that retain biochemical activity. Variability hot-spot mutations that reduce inhibitor potency are likely to identify direct inhibitor–target interactions and can be used to optimize compound potency and selectivity. Testing compounds against wild-type and mutant alleles can help select the most likely inhibitor–target binding mode from the solutions yielded by computational docking methods (Fig. 6).

We speculate that selective chemical probes for AAA proteins could be designed by engineering interactions with unique combinations of variability hot-spot residues. The core structures of compounds that bind conserved structural features of ATPases can be used as starting scaffolds to which different chemical groups may be added to contact the variability hot-spot residues in the target AAA protein. For instance, pyrazolyl-heterocycle-based scaffolds are likely to be valuable starting points for developing inhibitors of katanin, a microtubule-severing AAA protein closely related to spastin. In katanin the P-loop and N-loop variability hot-spot residues are threonine and leucine, respectively, compared with asparagine and glutamine at equivalent sites in spastin, and engineering contacts with these residues could lead to katanin-specific chemical probes. For AAA proteins in which the shape of the nucleotide-binding site and the variability hot-spot residues diverge more substantially from spastin, other core scaffolds may be needed. Mutant AAA protein alleles can be generated, and their inhibition by these scaffolds could be tested to develop models for inhibitor–target binding and guide compound optimization. These analyses would also help identify cognate inhibitor resistance-conferring mutations that can be used along with the inhibitor to decipher target-specific phenotypes in cells (Fig. 6).

In principle, the mutagenesis-based approach we used to develop spastazoline could help design inhibitors of targets for which high-resolution structural data for inhibitor–protein interactions are not readily available, or the inhibitor-bound conformation states are not known. Additional studies will be needed to determine whether variability hot-spot residues can be identified and swapped to design functionally silent mutations for protein–protein interactions or other nonenzymatic sites that can be targeted by chemical inhibitors.

Identifying and analyzing resistance-conferring mutations at an early stage of inhibitor design may also help develop chemical therapeutics against which resistance is less likely to arise.

## Online content

Any methods, additional references, Nature Research reporting summaries, source data, statements of data availability and associated accession codes are available at https://doi.org/10.1038/s41589-019-0225-6.

Received: 25 July 2018; Accepted: 21 December 2018;
Published online: 18 February 2019

## References

1. Erzberger, J. P. & Berger, J. M. Evolutionary relationships and structural mechanisms of AAA+ proteins. *Annu. Rev. Biophys. Biomol. Struct.* **35**, 93–114 (2006).
2. Lampson, M. A. & Kapoor, T. M. Unraveling cell division mechanisms with small-molecule inhibitors. *Nat. Chem. Biol.* **2**, 19–27 (2006).
3. Chou, T. F. et al. Reversible inhibitor of p97, DBeQ, impairs both ubiquitin-dependent and autophagic protein clearance pathways. *Proc. Natl Acad. Sci. USA* **108**, 4834–4839 (2011).
4. Firestone, A. J. et al. Small-molecule inhibitors of the AAA+ ATPase motor cytoplasmic dynein. *Nature* **484**, 125–129 (2012).
5. Kawashima, S. A. et al. Potent, reversible, and specific chemical inhibitors of eukaryotic ribosome biogenesis. *Cell* **167**, 512–524.e14 (2016).
6. Magnaghi, P. et al. Covalent and allosteric inhibitors of the ATPase VCP/p97 induce cancer cell death. *Nat. Chem. Biol.* **9**, 548–556 (2013).
7. Roll-Mecak, A. & McNally, F. J. Microtubule-severing enzymes. *Curr. Opin. Cell Biol.* **22**, 96–103 (2010).
8. Roll-Mecak, A. & Vale, R. D. The *Drosophila* homologue of the hereditary spastic paraplegia protein, spastin, severs and disassembles microtubules. *Curr. Biol.* **15**, 650–655 (2005).
9. McNally, F. J. & Vale, R. D. Identification of katanin, an ATPase that severs and disassembles stable microtubules. *Cell* **75**, 419–429 (1993).
10. Sharp, D. J. & Ross, J. L. Microtubule-severing enzymes at the cutting edge. *J. Cell. Sci.* **125**, 2561–2569 (2012).
11. Allison, R. et al. An ESCRT-spastin interaction promotes fission of recycling tubules from the endosome. *J. Cell. Biol.* **202**, 527–543 (2013).
12. Allison, R. et al. Defects in ER-endosome contacts impact lysosome function in hereditary spastic paraplegia. *J. Cell. Biol.* **216**, 1337–1355 (2017).
13. Vietri, M. et al. Spastin and ESCRT-III coordinate mitotic spindle disassembly and nuclear envelope sealing. *Nature* **522**, 231–235 (2015).
14. Kuo, T. C. et al. Purine-type compounds induce microtubule fragmentation and lung cancer cell death through interaction with katanin. *J. Med. Chem.* **59**, 8521–8534 (2016).
15. Banerjee, S. et al. 2.3 Å resolution cryo-EM structure of human p97 and mechanism of allosteric inhibition. *Science* **351**, 871–875 (2016).
16. Pöhler, R. et al. A non-competitive inhibitor of VCP/p97 and VPS4 reveals conserved allosteric circuits in type I and II AAA ATPases. *Angew. Chem. Int. Ed. Engl.* **57**, 1576–1580 (2018).
17. Beyer, A. Sequence analysis of the AAA protein family. *Protein Sci.* **6**, 2043–2058 (1997).
18. Puchades, C. et al. Structure of the mitochondrial inner membrane AAA+ protease YME1 gives insight into substrate processing. *Science* **358**, eaao0464 (2017).
19. Davis, A. M., Teague, S. J. & Kleywegt, G. J. Application and limitations of X-ray crystallographic data in structure-based ligand and drug design. *Angew. Chem. Int. Ed. Engl.* **42**, 2718–2736 (2003).
20. Han, T. et al. Anticancer sulfonamides target splicing by inducing RBM39 degradation via recruitment to DCAF15. *Science* **356**, eaal3755 (2017).
21. Wacker, S. A., Houghtaling, B. R., Elemento, O. & Kapoor, T. M. Using transcriptome sequencing to identify mechanisms of drug action and resistance. *Nat. Chem. Biol.* **8**, 235–237 (2012).
22. Kapoor, T. M. & Miller, R. M. Leveraging chemotype-specific resistance for drug target identification and chemical biology. *Trends Pharmacol. Sci.* **38**, 1100–1109 (2017).
23. Anderson, D. J. et al. Targeting the AAA ATPase p97 as an approach to treat cancer through disruption of protein homeostasis. *Cancer Cell* **28**, 653–665 (2015).
24. Roll-Mecak, A. & Vale, R. D. Structural basis of microtubule severing by the hereditary spastic paraplegia protein spastin. *Nature* **451**, 363–367 (2008).
25. Rouiller, I. et al. Conformational changes of the multifunction p97 AAA ATPase during its ATPase cycle. *Nat. Struct. Biol.* **9**, 950–957 (2002).
26. Ye, Q. et al. TRIP13 is a protein-remodeling AAA+ ATPase that catalyzes MAD2 conformation switching. *eLife* **4**, e07367 (2015).
27. Loughlin, R., Wilbur, J. D., McNally, F. J., Nédélec, F. J. & Heald, R. Katanin contributes to interspecies spindle length scaling in Xenopus. *Cell* **147**, 1397–1407 (2011).
28. Karlberg, T. et al. Crystal structure of human fidgetin-like protein 1 in complex with ADP. https://doi.org/10.2210/pdb3D8B/pdb (2008).
29. Whitehead, E., Heald, R. & Wilbur, J.D. N-terminal phosphorylation of p60 katanin directly regulates microtubule severing. *J. Mol. Biol.* **425**, 214–221 (2013).
30. Taylor, J. L., White, S. R., Lauring, B. & Kull, F. J. Crystal structure of the human spastin AAA domain. *J. Struct. Biol.* **179**, 133–137 (2012).
31. Amaro, R. E. et al. Ensemble docking in drug discovery. *Biophys. J.* **114**, 2271–2278 (2018).
32. Statsuk, A. V. et al. Tuning a three-component reaction for trapping kinase substrate complexes. *J. Am. Chem. Soc.* **130**, 17568–17574 (2008).
33. Claudiani, P., Riano, E., Errico, A., Andolfi, G. & Rugarli, E. I. Spastin subcellular localization is regulated through usage of different translation start sites and active export from the nucleus. *Exp. Cell Res.* **309**, 358–369 (2005).
34. Connell, J. W., Lindon, C., Luzio, J. P. & Reid, E. Spastin couples microtubule severing to membrane traffic in completion of cytokinesis and secretion. *Traffic* **10**, 42–56 (2009).
35. Mierzwa, B. E. et al. Dynamic subunit turnover in ESCRT-III assemblies is regulated by Vps4 to mediate membrane remodelling during cytokinesis. *Nat. Cell Biol.* **19**, 787–798 (2017).
36. Schellhaus, A. K., De Magistris, P. & Antonin, W. Nuclear reformation at the end of mitosis. *J. Mol. Biol.* **428**, 1962–1985 (2016).
37. Yang, D. et al. Structural basis for midbody targeting of spastin by the ESCRT-III protein CHMP1B. *Nat. Struct. Mol. Biol.* **15**, 1278–1286 (2008).
38. Olmos, Y., Hodgson, L., Mantell, J., Verkade, P. & Carlton, J. G. ESCRT-III controls nuclear envelope reformation. *Nature* **522**, 236–239 (2015).
39. Blackstone, C., O'Kane, C. J. & Reid, E. Hereditary spastic paraplegias: membrane traffic and the motor pathway. *Nat. Rev. Neurosci.* **12**, 31–42 (2011).
40. Zempel, H. et al. Amyloid-β oligomers induce synaptic damage via Tau-dependent microtubule severing by TTLL6 and spastin. *EMBO J.* **32**, 2920–2937 (2013).

## Acknowledgements

We thank J. Steinman and P. Verma for help with AAA protein purification, and M. Grasso for the purification of human VPS4B. We thank F. Glickman and C. Adura of the Rockefeller University High-Throughput and Spectroscopy Resource Center for assistance with assay development and A. North of the Rockefeller Bioimaging Resource Center. We are especially grateful to L. Kapitein, K. Jansen and W. Nijenhuis (Utrecht University) for testing our spastin inhibitors in cellular assays. We are also grateful to R. Heald (University of California, Berkeley) and C. Campsteijn (Oslo University Hospital) for plasmids and to A. Roll-Mecak (NIH) for a plasmid and a protein sample for the initial assay validation. T.C. was supported by the EMBO Long-Term Fellowship for post-doctoral studies and by the Kestenbaum award for research in neurodegenerative diseases. M.E.K. acknowledges support from an NIH training grant (GM066699). T.M.K. is grateful to the NIH (GM98578) for supporting this research.

## Authors contributions

T.C., R.P., and T.M.K. conceived the project and designed experiments. T.C. and R.P. synthesized compounds, performed assays, and analyzed data. M.E.K. performed western blot analyses and assisted with cell imaging experiments and data analysis. T.M.K. supervised the research. T.C. and T.M.K. wrote the manuscript with input from all authors.

## Competing interests

The authors declare no competing interests.

## Additional information

**Supplementary information** is available for this paper at https://doi.org/10.1038/s41589-019-0225-6.

**Reprints and permissions information** is available at www.nature.com/reprints.

**Correspondence and requests for materials** should be addressed to T.M.K.

**Publisher's note:** Springer Nature remains neutral with regard to jurisdictional claims in published maps and institutional affiliations.

## Methods

**Plasmids.** Human (Hs-spastin) and *D. melanogaster* spastin (Dm-spastin) vectors. Hs-spastin can be expressed as at least four isoforms (M1 with exon 4, M1 without exon 4, M87 with exon 4, and M87 without exon 4)[41]. Vectors for mutant constructs were generated by site-directed mutagenesis (QuikChange XL Kit, Agilent, catalog no. 200517). Incorporation of the desired mutations was verified by Sanger sequencing.

The wild-type (WT, isoform M87 with exon 4, with N-terminal HA- and EGFP-tags) spastin plasmid used to generate cell lines was a gift from C. Campsteijn (Oslo University Hospital). Wild-type and mutant spastin M87e4 open reading frames were subcloned into the pcDNA 5.0/FRT/TO vector (ThermoFisher) using *Hin*dIII and *Not*I restriction sites. The complementary DNA sequence for Hs-spastin (residues 229–616, numbered according to NCBI RefSeq: NP_055761.2) used for protein expression was PCR amplified from the ORFeome collection (Dharmacon) and cloned into a pGEX-6P1 vector using *Bam*HI and *Not*I restriction sites.

The vector (pDEST15-spastin-*D.melanogaster*) used for Dm-spastin expression was a gift from A. Roll-Mecak (NIH) and had been previously used in ref. [24]. We note that in this construct, consisting of residues 209–758, there is a deletion at residues 311–372 (corresponding to exon 3 of *Drosophila* spastin). However, the overall residue numbering used is that for full-length Dm-spastin isoform A (Uniprot: Q8I0P1), as in previous publications[24].

*Xenopus laevis katanin vector.* MAL-c5x-*X.laevis* p60 (full length, NCBI RefSeq: NP_001084226.1) was a gift from R. Heald (UC Berkeley).

*Mus musculus VCP vector.* pQE9-His-p97 (identical to *Homo sapiens* VCP protein, full length, NCBI RefSeq: NP_009057.1, Ile206Val variant) was obtained from Addgene (G. Warren, plasmid #14666).

*Homo sapiens PCH2 vector.* The cDNA for Hs-PCH2 (full length, NCBI RefSeq: NP_004228) was PCR amplified from the ORFeome collection and cloned using the *Apa*I and *Asc*I restriction sites into a pDEST15 vector.

*Homo sapiens FIGL1 vector.* The cDNA for Hs-FIGL1 (residues 288–674, NCBI RefSeq: NP_001036227.1) was PCR amplified from the ORFeome collection and cloned into a pDEST15 vector using the *Apa*I site and InFusion technology (Clontech).

*Homo sapiens VPS4B vector.* The cDNA for the sequence Hs-VPS4B (full length, NCBI RefSeq: BC039574.1) was PCR amplified from the ORFeome collection and cloned using the *Nde*I and *Eco*RI restriction sites into a pET-SUMO vector.

**Cell lines, cell culture, and viability analyses.** Cells expressing wild type- or mutant-tagged spastin M87e4 were generated using the T-REx HeLa Flp-In cell line according to the vendor's protocols (ThermoFisher). Genomic DNA was extracted from cells using the DNeasy Blood and Tissue kit (Qiagen), insertions were PCR amplified and sequenced. Cells were cultured in DMEM (ThermoFisher) supplemented with 10% (v/v) FBS (Sigma-Aldrich), L-glutamine (2 mM; Thermo Fisher), hygromycin B (250 μg ml$^{-1}$) and blasticidin (20 μg ml$^{-1}$) at 37 °C and 5% $CO_2$. Cells were confirmed to be mycoplasma free using a PCR-based method[42].

For western blotting, cells were cultured with or without doxycycline (1 μg ml$^{-1}$ for 24 h) before lysis at 4 °C. The following antibodies were used: mouse monoclonal anti-spastin (1:750; Sp6C6; Abcam) and goat polyclonal anti-GAPDH (control, 1:1,000; V-18; Santa Cruz). Membranes were imaged using a LI-COR Odyssey Infrared Imager. Cell viability assays were conducted using a CellTiter-Glo Luminescent Cell Viability Assay (Promega) according to the manufacturer recommendations. The luminescence signal was quantified using a Synergy NEO Microplate Reader.

**Microscopy.** *Live-cell imaging.* HeLa-WT and N386C cells were grown on 22 mm × 22 mm coverslips and mounted in a custom Rose chamber in 10% FBS in L-15 media without phenol red (Invitrogen) and maintained at 35–37 °C. For inhibitor treatment, cells were incubated with spastazoline for 40 min before mounting and imaging.

Confocal GFP fluorescence micrographs were acquired using a Nikon TE2000 microscope (Morrell Instruments), with a 100× objective (Plan Apo, 1.45 NA), a Yokogawa CSU10 confocal head, and an EMCCD Photometrics Cascade II 512B camera (Roper Scientific). For the detection of GFP–spastin dots, the FIJI[43] ComDet v.0.3.7 plugin was used (https://github.com/ekatrukha/ComDet), which detects particles by applying a two-dimensional Gaussian Mexican hat filter to the original image, which was followed by thresholding, finding of maxima, segmentation, and centroid calculation. The quality of the automated detection was visually checked. This plugin was used to detect particles >2 pixels with a signal-to-noise ratio ranging from 1.05 to 3.

*Immunofluorescence analyses.* Cells were plated on acid-washed coverslips (#1.5; Fisher brand catalog no. 12-545-81) coated with poly-D-lysine hydrobromide (Sigma, catalog no. P6407) and cultured for 24–48 h before fixation.

For intercellular bridge analyses, spastin expression was induced (1 μg ml$^{-1}$ doxycycline for ~24 h), and cells were treated with 10 μM spastazoline or 0.1% DMSO (solvent control) for 4.5 h and then fixed at 37 °C, using 0.5% (w/v) glutaraldehyde in PBS for 10 min. Coverslips were washed with PBS, incubated with a solution of 0.1% $NaBH_4$ for 10 min, and blocked (blocking buffer: 2% bovine serum albumin, 0.1% (w/v) sodium azide, and 0.1% Triton X-100 in Tris-buffered saline) for 60 min. Cells were stained with mouse monoclonal anti-acetylated tubulin (Sigma catalog no. T7451; 1:1,000 dilution) for 2 h and with Texas-Red conjugated anti-mouse secondary antibody (Jackson Immunoresearch; catalog no. 715-075-020; 1:2,000 dilution) for 60 min. DNA was stained with Hoechst 33342 (ThermoFisher, catalog no. H1399).

For intercellular bridge quantification, 5 × 5 fields of view were acquired using a 40× objective (Plan Fluor, 0.6 NA) and stitched together into ~905 μm$^2$ images using NIS-Elements. The number of cells and intercellular bridges were detected manually.

For three-dimensional imaging of fixed cells, we used a DeltaVision Image Restoration Microscope (Applied Precision) with an Olympus IX-70 base and Resolve 3D softWoRx-Acquire acquisition software (v: 6.5.2, Release RC1). *Z*-stacks were collected with a 0.25 μm step size and images were deconvolved using softWoRx.

For microtubule staining, cells were treated with 10 μM spastazoline or 0.1% DMSO (solvent control) for 4 h and then fixed at 37 °C using 4% formaldehyde in 100 mM PIPES, 10 mM EGTA, 1 mM $MgCl_2$, and 0.2% Triton X-100, pH 6.9 for 10 min. Coverslips were blocked (blocking buffer) for 45 min before staining with anti-α-tubulin-FITC antibody (DM1A, Sigma, catalog no. F2168; 1:2,000 dilution). Confocal fluorescence images were acquired as *Z*-stacks with 0.3 μm step size using a Nikon TE2000 microscope with a 100× objective (Plan Apo, 1.45 NA).

**Biochemical assays.** *Recombinant protein expression.* Recombinant proteins were expressed in *Escherichia coli* Rosetta (DE3) pLysS cells (Merck, catalog no. 70954) grown in Miller's LB medium (LMM, Formedium, catalog no. LMM105). For all constructs, protein expression was induced at $A_{600}$ = 0.6–0.8 with 0.5 mM IPTG (Goldbio). The cultures were grown at 18 °C for 12–16, pelleted, and resuspended in lysis buffer (buffer A, see below). All subsequent purification steps were performed at 4 °C. Cell lysis was carried out using an Emulsiflex-C5 homogenizer (Avestin, 5–6 cycles at 10,000–15,000 psi). The homogenized lysate was centrifuged at 40,000 r.p.m. for 45–60 min using a Ti45 rotor in a Beckman Coulter Optima LE-80K ultracentrifuge. All recombinant proteins were purified using multistep strategies, involving combinations of affinity, ion exchange, and size-exclusion chromatography. Specific buffers and purification conditions, optimized for yield and specific activity, are summarized.

*Dm-spastin wild type and mutants.* Buffer A: PBS, 10 mM $MgCl_2$, 1 mM PMSF, 20 U ml$^{-1}$ benzonase, and cOmplete EDTA-Free Protease Inhibitor Cocktail. Buffer B1: 50 mM Tris–HCl, 500 mM KCl, 10 mM $MgCl_2$, 5 mM DTT, pH 7.5. Buffer B2: 50 mM Tris–HCl, 300 mM NaCl, 10 mM $MgCl_2$, 5 mM DTT, 20 mM reduced glutathione, pH 8.0. Buffer C: 50 mM Na-MES, 10% (w/v) glycerol, 10 mM $MgCl_2$, 5 mM DTT, pH 6.5. Buffer D: 50 mM Na-MES, 2 M NaCl, 10% (w/v) glycerol, 10 mM $MgCl_2$, 5 mM DTT, pH 6.5. Buffer E: 20 mM K-HEPES, 300 mM NaCl, 10 mM $MgCl_2$, 5 mM DTT, 15% (w/v) glycerol, pH 7.5.

*Conditions.* Briefly, the clarified lysate containing GST–Dm-spastin was incubated with a GSTrap 4B matrix (GE Healthcare) and eluted in Buffer B2. The protein solution was incubated with PreScission protease (0.1 mg ml$^{-1}$) for 8–12 h, diluted 1:2.5 with Buffer C and loaded into a CaptoS cation exchange column (GE Healthcare) equilibrated in 95% Buffer C and 5% Buffer D. Fractions eluted from the ion exchange chromatography column were pooled, concentrated tenfold with an Amicon Ultra 30K MWCO centrifugal filter, and further purified over a 16/60 Superdex 200 column (GE Healthcare) in Buffer E. The eluate containing purified spastin was pooled, concentrated using an Amicon Ultra 30K MWCO centrifugal filter to at least 1 mg ml$^{-1}$ and stored at −80 °C. PreScission cleavage left six nonnative residues at the N terminus (GPQGSK).

*Hs-spastin wild type and N386C mutant.* Buffer A: PBS, 10 mM $MgCl_2$, 10 mM DTT, 1 mM PMSF, 5 U ml$^{-1}$ benzonase, and cOmplete EDTA-Free Protease Inhibitor Cocktail, pH 7.4. Buffer B: 50 mM K-HEPES, 250 mM KCl, 5 mM $MgCl_2$, 5 mM DTT, 0.1 mM PMSF, 0.005% (v/v) Triton X-100, pH 7.5. Buffer C: 50 mM Na-MES, 10% (w/v) glycerol, 5 mM $MgCl_2$, 5 mM DTT, pH 6.5. Buffer D: 50 mM Na-MES, 2 M NaCl, 10% (w/v) glycerol, 5 mM $MgCl_2$, 5 mM DTT, pH 6.5.

*Conditions.* Briefly, the clarified lysate containing GST–Hs-spastin was incubated with a GSTrap 4B matrix (GE Healthcare) and eluted in Buffer B supplemented with 20 mM reduced glutathione. The protein solution was incubated with PreScission protease (0.1 mg ml$^{-1}$) for 10–12 h, diluted 1:2 with Buffer C and loaded into a CaptoS cation exchange column (GE Healthcare) equilibrated in 93% Buffer C and 7% Buffer D. Fractions eluted from the ion exchange chromatography column were pooled and concentrated tenfold with an Amicon Ultra 50K MWCO centrifugal filter. The protein solution was centrifuged at 20,000*g* for 15 min, and the soluble fraction was stored at −80 °C. PreScission cleavage left five nonnative residues at the N terminus (GPLGS).

*GST-FIGL1 (Hs-FIGL1).* Hs-FIGL1 protein used for measurement of kinetic parameters was obtained by the following procedure (Method 1): Buffer A: 25 mM Tris–HCl, 300 mM NaCl, 5 mM $MgCl_2$, 5 mM DTT, 1 mM PMSF, 0.01% (v/v) Triton X-100, and cOmplete EDTA-Free Protease Inhibitor Cocktail, pH 8.0. Buffer B1: 25 mM Tris–HCl, 300 mM NaCl, 5 mM $MgCl_2$, 5 mM DTT, 0.4 mM PMSF, 0.01% (v/v) Triton X-100, pH 8.0. Buffer B2: 25 mM Tris–HCl, 150 mM NaCl, 5 mM $MgCl_2$, 5 mM DTT, 10 mM reduced glutathione, pH 8. Buffer C: 25 mM Tris–HCl, 75 mM NaCl, 5 mM $MgCl_2$, 5 mM DTT, pH 8.5. Buffer D: 25 mM Tris–HCl, 500 mM NaCl, 5 mM $MgCl_2$, 5 mM DTT, pH 8.5. Buffer E: 25 mM Tris–HCl, 150 mM NaCl, 5 mM $MgCl_2$, 5 mM DTT, 5% (w/v) glycerol, pH 7.5

*Conditions.* The clarified lysate from cells expressing GST-FIGL1 was loaded onto GSTrap 4B (GE Healthcare), washed with Buffer B1 and then Buffer D, and finally eluted with Buffer B2. Fractions containing the proteins were pooled, diluted with 1 volume of Buffer C, and loaded on a MonoQ 5/50 GL column (GE Healthcare), equilibrated in 95% Buffer C and 5% Buffer D. The protein fractions were pooled, concentrated tenfold using an Amicon Ultra 50K MWCO centrifugal filter, and further purified over a 10/300 Superdex 200 column (GE Healthcare) in Buffer E. Fractions from size-exclusion column were concentrated to a minimum of 1 mg ml$^{-1}$ using an Amicon Ultra 30K MWCO centrifugal filter, and stored at −80 °C.

Method 2: Buffer A: 50 mM Tris–HCl, 150 mM NaCl, 5 mM $MgCl_2$, 10 mM DTT, 0.1 mM PMSF, 0.01% (v/v) Triton X-100, 5 U ml$^{-1}$ benzonase, and cOmplete EDTA-Free Protease Inhibitor Cocktail, pH 8.0. Buffer B1: 25 mM Tris–HCl, 300 mM NaCl, 5 mM $MgCl_2$, 5 mM DTT, 0.1 mM PMSF, 0.01% (v/v) Triton X-100, pH 8.0. Buffer B2: 25 mM Tris–HCl, 150 mM NaCl, 5 mM $MgCl_2$, 5 mM DTT, 10 mM reduced glutathione, pH 8.0. Buffer C: 25 mM Tris–HCl, 75 mM NaCl, 5 mM $MgCl_2$, 5 mM DTT, pH 8.5. Buffer D: 25 mM Tris–HCl, 1 M NaCl, 5 mM $MgCl_2$, 5 mM DTT, pH 8.5. Buffer E: 25 mM Tris–HCl, 150 mM NaCl, 5 mM $MgCl_2$, 5 mM DTT, 5% (w/v) glycerol, pH 7.5.

*Conditions.* The clarified lysate from cells expressing GST-FIGL1 was incubated with sepharose glutathione beads (GE Healthcare) for 1 h, washed with Buffer B1 and eluted with Buffer B2. Fractions containing the protein were pooled, diluted with three volumes of Buffer C, and loaded on a MonoQ 5/50 GL column (GE Healthcare), equilibrated in 95% Buffer C and 5% Buffer D. The protein fractions were pooled, concentrated tenfold using an Amicon® Ultra 50K MWCO centrifugal filter, and further purified over a 10/300 Superdex 200 column (GE Healthcare) in Buffer E. Fractions from size-exclusion column were concentrated to a minimum of 1 mg ml$^{-1}$ using an Amicon Ultra 30K MWCO centrifugal filter, and stored at −80 °C. Hs-FIGL1 protein used for testing inhibitors was obtained with method 1 or method 2. We note that protein purity and ATPase activity were comparable between the methods (data not shown).

*MBP-katanin (Xl-katanin).* Buffer A: 20 mM Tris–HCl, 250 mM NaCl, 5 mM $MgCl_2$, 100 µM ATP, 5 mM DTT, 10% (w/v) glycerol, 1 mM PMSF, and cOmplete EDTA-Free Protease Inhibitor Cocktail, pH 7.5. Buffer B: 20 mM Tris–HCl, 250 mM NaCl, 5 mM $MgCl_2$, 100 µM ATP, 5 mM DTT, 10% (w/v) glycerol, pH 7.5. Buffer C: 20 mM Tris–HCl, 50 mM NaCl, 1 mM $MgCl_2$, 5 mM DTT, 100 µM ATP, 10% (w/v) glycerol, pH 7.5. Buffer D: 20 mM Tris–HCl, 500 mM NaCl, 5 mM $MgCl_2$, 5 mM DTT, 100 µM ATP, 10% (w/v) glycerol, pH 7.5. Buffer E: 20 mM Na-HEPES, 250 mM NaCl, 5 mM $MgCl_2$, 5 mM DTT, 10% (w/v) glycerol, pH 7.5.

*Conditions.* The clarified lysate from cells expressing MBP-katanin was loaded onto an MBP trap column (GE Healthcare). The column was washed with 30 column volumes of Buffer B and eluted with a Buffer B supplemented with 10 mM maltose. The eluate was diluted 1:2 with Buffer C and loaded on a 16/60 MonoQ GL ion exchange column and eluted with a gradient of Buffer D. Combined MonoQ fractions were further purified on a 10/300 Superdex 200 gel filtration column in Buffer E. The fractions containing purified MBP-katanin protein were frozen in liquid nitrogen and stored at −80 °C.

*VCP (Mm-VCP).* Mm-VCP protein used for measurement of kinetic parameters was obtained by the following procedure (Method 1): Buffer A: 25 mM K-HEPES, 500 mM KCl, 20 mM imidazole, 2 mM DTT, 5 U ml$^{-1}$ benzonase, and cOmplete EDTA-Free Protease Inhibitor Cocktail, pH 8.0. Buffer B: 25 mM K-HEPES, 500 mM KCl, 20 mM imidazole, 2 mM DTT, pH 8.0. Buffer C: 25 mM K-HEPES, 500 KCl, 1 mM $MgCl_2$, 2 mM DTT, 500 mM imidazole, pH 7.5. Buffer D: 25 mM K-HEPES, 250 mM KCl, 1 mM $MgCl_2$, 2 mM DTT, pH 7.5.

*Conditions.* The clarified lysate from cells expressing His6-VCP was incubated with Ni-NTA beads (Qiagen) for 40 min, and the beads were extensively washed using Buffer B. The protein was eluted with Buffer C. Fractions containing the protein were concentrated using an Amicon Ultra 50K MWCO centrifugal filter, and the concentrated protein sample was filtered through a 0.22-µm Millex-GP PES membrane and loaded on a 10/300 Superose 6 column (GE Healthcare) in Buffer D. Fractions from the size-exclusion column were concentrated using an Amicon Ultra 50K MWCO centrifugal filter, and the concentrated protein sample was stored at −80 °C.

Method 2: Buffer A: 50 mM Tris–HCl, 400 mM NaCl, 2 mM $MgCl_2$, 20 mM imidazole, 1 mM ATP, 2 mM tris(2-carboxyethyl)phosphine (TCEP), 0.025% (v/v) Triton X-100, and cOmplete EDTA-Free Protease Inhibitor Cocktail, pH 7.5 (at 25 °C). Buffer B: 50 mM Tris–HCl, 300 mM NaCl, 40 mM imidazole, 5 mM $MgCl_2$, 1 mM TCEP, 0.01% (v/v) Triton X-100, pH 7.5 (at 25 °C). Buffer C: 50 mM Na-HEPES, 100 mM NaCl, 5 mM $MgCl_2$, 1 mM TCEP, pH 7.5 (at 25 °C). Buffer D: 50 mM Na-HEPES, 1 M NaCl, 5 mM $MgCl_2$, 1 mM TCEP, pH 7.5 (at 25 °C). Buffer E: 50 mM Na-HEPES, 300 mM NaCl, 5 mM $MgCl_2$, 1 mM TCEP, pH 7.5 (at 25 °C).

*Conditions.* The clarified lysate in buffer A from cells expressing His6-VCP was incubated with Ni-NTA beads (Qiagen) for 40 min, and the beads were extensively washed with Buffer B. The protein was eluted with Buffer B supplemented with 500 mM imidazole. Eluted fractions were pooled and dialyzed in Buffer C. After dialysis, the protein was loaded onto a MonoQ column 5/50 GL (GE Healthcare) and fractioned over a gradient with Buffer D. Protein was eluted at approximately 350 mM NaCl. Combined MonoQ fractions were concentrated using an Amicon Ultra 50K MWCO centrifugal filter, and the concentrated protein sample was filtered through a 0.22-µm Millex-GP PES membrane before loading onto a 10/300 Superdex 200 column (GE Healthcare) equilibrated in Buffer E. Fractions from the size-exclusion column were concentrated using an Amicon Ultra 50K MWCO centrifugal filter, and the concentrated protein sample was mixed with 15% (w/v) glycerol and stored at −80 °C. Mm-VCP protein used for testing inhibitors was obtained with method 1 or method 2. We note that protein purity and ATPase activity were comparable between the methods (data not shown).

*PCH2 (Hs-PCH2).* Buffer A: 50 mM Tris–HCl, 250 mM NaCl, 10 mM $MgCl_2$, 5 mM DTT, 1.2 mM PMSF, 0.02% (v/v) Triton X-100, 0.5 mM MgATP, 1 mM EGTA, 5 U ml$^{-1}$ benzonase, and cOmplete EDTA-Free Protease Inhibitor Cocktail, pH 7.5. Buffer B1: 25 mM Tris–HCl, 350 mM NaCl, 10 mM $MgCl_2$, 5 mM DTT, 0.2 mM MgATP, 0.02% (v/v) Triton X-100, 1 mM EGTA, pH 8.0. Buffer B2: 25 mM Tris–HCl, 150 mM NaCl, 10 mM $MgCl_2$, 5 mM DTT, 20 µM reduced glutathione, 0.5 mM EGTA, pH 8.0. Buffer E: 25 mM Tris–HCl, 150 mM NaCl, 5 mM $MgCl_2$, 5 mM DTT, 10% (w/v) glycerol, pH 8.0.

*Conditions.* The clarified lysate from cells expressing GST-PCH2 was incubated with sepharose glutathione beads (GE Healthcare) for 1 h, and the beads were washed with 50 volumes of Buffer B1 followed by 10 volumes of Buffer B2. PreScission protease (0.1 mg ml$^{-1}$) was added, and the beads were incubated for 12 h. The protein-containing solution was recovered by filtration and incubated with fresh sepharose glutathione beads for 1 h. Beads were removed by centrifugation at 1,440 r.p.m. using an Allegra X30-R centrifuge and the solution was concentrated 20-fold using an Amicon Ultra 30K MWCO centrifugal filter, filtered through a 0.33-µm Millex-GP PES membrane and further purified over a 10/300 Superdex 75 column (GE Healthcare) in Buffer E. Fractions containing purified protein from the size-exclusion column were concentrated to a minimum of 1 mg ml$^{-1}$ using an Amicon Ultra 30K MWCO centrifugal filter and stored at −80 °C.

*6XHis-SUMO-VPS4B (Hs-VPS4B).* Buffer A: 20 mM Na-HEPES, 500 mM NaCl, 2 mM $MgCl_2$, 10% (w/v) glycerol, 0.5 mM DTT, 1 mM PMSF, 1 mM ATP, and cOmplete EDTA-Free Protease Inhibitor Cocktail, pH 7.6. Buffer B1: 20 mM Na-HEPES, 500 mM NaCl, 2 mM $MgCl_2$, 0.5 mM DTT, 1 mM PMSF, 1 mM ATP, 15 mM imidazole, pH 7.6. Buffer B2: 20 mM Na-HEPES, 500 mM NaCl, 2 mM $MgCl_2$, 0.5 mM DTT, 1 mM PMSF, 1 mM ATP, 400 mM imidazole, pH 7.6. Buffer C: 25 mM Na-HEPES, 2 mM $MgCl_2$, 1 mM DTT, pH 7.6. Buffer D: 25 mM Na-HEPES, 1 M NaCl, 2 mM $MgCl_2$, 1 mM DTT, pH 7.6. Buffer E: 50 mM Na-HEPES, 150 mM NaCl, 3 mM $MgCl_2$, 2 mM DTT, pH 7.6.

*Conditions.* The clarified lysate from cells expressing 6xHIS-SUMO-VPS4B was incubated with Ni-NTA beads for 1 h, and the beads were washed with 10 volumes of Buffer A and then 10 volumes of Buffer B1, and eluted with 10 volumes of Buffer B2. The protein-containing solution was diluted with 2.5 volumes of diluted Buffer A (1:1 in $H_2O$), loaded onto a MonoQ column 5/50 GL (GE Healthcare) equilibrated in Buffer C, and fractioned over a gradient with Buffer D. Combined MonoQ fractions were concentrated using an Amicon Ultra 30K MWCO centrifugal filter, and the concentrated protein sample was filtered through a 0.22-µm Millex-GP PES membrane before loading onto a 10/200 Superdex 200 column (GE Healthcare) equilibrated in Buffer E. Fractions from size-exclusion column were concentrated using an Amicon Ultra 30K MWCO centrifugal filter and concentrated protein sample was mixed with 10% (w/v) glycerol and stored at −80 °C.

*Analyses of ATPase activity.* Steady-state ATPase activity of AAA proteins was determined using the NADH-coupled assay. For all analyses, the time course of fluorescence decrease was measured using a Synergy NEO Microplate Reader ($\lambda_{ex}$ = 340 nm, 440 nm emission filter). The rate from a control reaction with no ATP (background rate of fluorescence decrease) was subtracted from all rates. The assay buffers were based on literature precedents, as available[3,25,29].

*Assay conditions for $K_{1/2}$ and $k_{cat}$ analyses (enzyme concentrations).* Dm-spastin wild-type and mutants (85 nM): 25 mM K-HEPES pH 7.5, 225 mM KCl, 25 mM $K_2HPO_4$, 5 mM $MgCl_2$, 2.5 mM DTT, 175 µM NADH.

Hs-spastin wild type and mutants (100 nM): 25 mM K-HEPES pH 7.5, 225 mM KCl, 25 mM $K_2HPO_4$, 5 mM $MgCl_2$, 2.5 mM DTT, 200 µM NADH.

Xl-katanin (80 nM): 25 mM K-HEPES pH 7.5, 70 mM KCl, 25 mM $K_2HPO_4$, 5 mM $MgCl_2$, 2.5 mM DTT, 175 µM NADH.

Hs-FIGL1 (50 nM): 25 mM Na-MES pH 6.5, 70 mM KOAc, 25 mM $K_2HPO_4$, 5 mM $Mg(OAc)_2$, 1 mM TCEP, 175 µM NADH.

Mm-VCP (450 nM): 25 mM K-HEPES pH 7.5, 25 mM KCl, 25 mM $K_2HPO_4$, 15 mM $MgCl_2$, 1 mM TCEP, 100–125 µM NADH.

Hs-PCH2 (340 nM): 25 mM Tris–HCl pH 8.5, 150 mM KCl, 25 mM $K_2HPO_4$, 5 mM $MgCl_2$, 2.5 mM DTT, 0.025% (v/v) Triton X-100, 125 µM NADH.

Each buffer also contained 0.1 mg ml$^{-1}$ BSA, 1 mM phosphoenolpyruvate, 40 U ml$^{-1}$ lactate dehydrogenase, and 40 U ml$^{-1}$ pyruvate kinase.

*Assay conditions for analysis of chemical inhibitors.* While testing compounds we observed some precipitation, which we found to be dependent on buffer conditions. Replacing $K_2HPO_4$ with $(NH_4)_2SO_4$ addressed this issue. As Dm-spastin is more active than Hs-spastin, 0.5 mM MgATP was used rather than 1 mM MgATP. For each assay we included Triton X-100 to prevent non-specific aggregation[44].

Dm-spastin wild-type and mutants: protein 70–100 nM, 25 mM K-HEPES pH 7.5, 200 mM KCl, 20 mM $(NH4)_2SO_4$, 5 mM $MgCl_2$, 2.5 mM DTT, 175 µM NADH.

Hs-spastin wild-type and mutants: protein 50 nM, 25 mM K-HEPES pH 7.5, 225 mM KCl, 2.5 mM $(NH4)_2SO_4$, 5 mM $MgCl_2$, 2.5 mM DTT, 0.005% w/v Triton X-100, 175 µM NADH.

Xl-katanin: protein 70 nM, 25 mM K-HEPES pH 7.5, 70 mM KCl, 20 mM $(NH_4)_2SO_4$, 5 mM $MgCl_2$, 2.5 mM DTT, 0.005% w/v Triton X-100, 150 µM NADH.

Hs-FIGL1: protein 50–70 nM, 25 mM Na-MES pH 6.5, 70 mM KOAc, 20 mM $(NH_4)_2SO_4$, 5 mM $Mg(OAc)_2$, 1 mM TCEP, 0.005% w/v Triton X-100, 150 µM NADH.

Mm-VCP: protein 300 nM, 50 mM K-HEPES pH 7.5, 25 mM KCl, 20 mM $(NH_4)_2SO_4$, 15 mM $MgCl_2$, 1 mM TCEP, pH 7.5, 100 µM NADH.

Hs-PCH2: protein 270 nM, 25 mM Tris–HCl pH 8.5, 150 mM KCl, 20 mM $(NH_4)_2SO_4$, 5 mM $MgCl_2$, 2.5 mM DTT, 0.025% (v/v) Triton X-100, 125 µM NADH.

Hs-VPS4B: protein 80 nM, 25 mM Na-HEPES pH 7.5, 25 mM KOAc, 2.5 mM $(NH_4)_2SO_4$, 2 mM $MgCl_2$, 1 mM TCEP, 0.01% (v/v) Triton X-100, 150 µM NADH.

Each buffer also contained: 0.1 mg ml$^{-1}$ BSA, 1 mM phosphoenolpyruvate, 30 U ml$^{-1}$ lactate dehydrogenase, 30 U ml$^{-1}$ pyruvate kinase.

*Equations used for data fitting.* Enzyme parameters $K_{1/2}$, $k_{cat}$, and Hill coefficients ($h$) for the recombinant enzymes were determined by fitting the rates to the Hill equation using Prism v. 6.0 (GraphPad Software Inc) at different ATP concentrations ($x$):

$$V = \text{ATPase rate} = \frac{V_{max}\, x^h}{K_{1/2}^h + x^h}$$

For each experiment the measured activity versus concentration of compound were plotted and data were fit using a sigmoidal dose–response curve equation in Prism to determine the half-maximum inhibitory concentration ($IC_{50}$).

$$Y = \%\ \text{ATPase rate relative to DMSO control} = (Y_{min}) + \frac{(Y_{max} + Y_{min})}{1 + 10^{\log IC_{50} - x}}$$

*Differential scanning fluorimetry.* These experiments were carried out on a C1000 Touch Thermal cycler CFX-96 instrument (GE Healthcare). Purified Hs-spastin wild-type or Hs-spastin N386C mutant were diluted to 16 µM in a buffer containing 50 mM $K_2HPO_4$, 200 mM KCl, 2 mM $MgCl_2$, and 2 mM DTT, pH 7.4. Spastazoline was diluted in this buffer supplemented with 4% (v/v) DMSO and SYPRO Orange (1:250 dilution), and an equal volume was added to the Hs-spastin solution (assay concentrations: compound, 6.25 µM to 200 µM; Hs-spastin, 8 µM; DMSO, 2%). Assays were conducted in a 96-well plate (Hard-shell HSP9665 Bio-Rad). The temperature was linearly increased with a step of 0.5 °C for 55 min, from 25 °C to 95 °C, and fluorescence readings were taken at each interval (excitation 490 nm, emission 590 nm). Melting temperatures were recorded as the minimum value of the first derivative of the fluorescence versus temperature curves.

*In vitro microtubule-severing assays.* A fluorescence-based assay was adapted from similar assays reported previously[45]. Briefly, X-rhodamine-labeled, taxol (Sigma, catalog no.T7402) -stabilized microtubules (bovine brain) were diluted in buffer A (20 mM K-HEPES, 30 mM KCl, 5 mM $MgCl_2$, 2 mM TCEP, 0.2 mg ml$^{-1}$ BSA, 0.01% Triton X-100). Compound **5** (2 µM, 1% DMSO final) and MgATP (0.5 mM) in buffer A were added and the mixture was incubated for 5 min. Dm-spastin was diluted to 150 nM in buffer B (50 mM K-HEPES, 300 mM KCl, 10 mM $MgCl_2$, 1 mM TCEP, 10% glycerol, 0.01% Triton X-100, pH 7.5) and then added to the mixture (final concentration: 15 nM). Aliquots were removed at selected time points, fixed, and imaged using a Zeiss Axiovert 200M wide-field microscope equipped with a Zeiss 100×/1.45 NA α-Plan Fluor objective and an EMCCD camera (iXon DU-897, Andor Technology).

**Computational methods.** *Analysis of nucleotide-binding sites of AAA proteins.* We used a three-dimensional structural alignment to compare the residue composition of the ATP-binding site in selected AAA proteins (Dm-spastin, Xl-katanin, Hs-FIGL1, Mm-VCP, and Hs-PCH2). We used available structural models for Dm-spastin (PDB: 3B9P), Hs-FIGL1 (PDB: 3D8B, chain A), the D1-AAA domain (PDB: 5FTK, chain A, residues 200–477), and the D2-AAA domain (residues 471–761) of human VCP. Since no structural models for katanin or human PCH2 were available at the beginning of these studies, homology models were generated for the ATPase domains of these proteins using Bioluminate (version 2.3, Schrödinger, LLC). Hs-PCH2 (residues 132–432, Uniprot reference sequence Q15645) was modeled using the structure of *Caenorhabditis elegans* PCH2 (PDB: 4XGU) as a template. Xl-katanin (residues 200–486, Uniprot reference sequence Q9PUL2) was modeled using 3D8B_A, 3VFD_A, and 3B9P_A as templates.

To identify the amino acid residues lining the adenine-binding pocket in these proteins the atom coordinates from the structural or homology models were aligned to the coordinates of ADP-bound Hs-FIGL1 using UCSF Chimera[46]. Hs-FIGL1 residues within 6 Å of the adenine were selected and the corresponding residues were identified in the ATPase domains of Dm-spastin, Xl-katanin, Mm-VCP, and Hs-PCH2, or in an extended set of 24 AAA proteins. These amino acid residues, along with the corresponding secondary structure motifs, are shown in Supplementary Fig. 1d,e.

*Inhibitor docking.* The molecular dynamics system was set up for Dm-spastin (PDB: 3B9P) using the Protein Preparation Wizard in Maestro (Schrödinger Release 2016.1). First, all non-protein atoms in the PDB file were kept, and the protein loops with no coordinates were modeled using Uniprot: Q8I0P1 as reference sequence. Hydrogen atoms were added to the protein structure, and the protonation states of ionizable residues were assigned for pH 7.0. This structure was neutralized with KCl ions, additional KCl ions were placed to reproduce a salt concentration of 0.15 M, and the system was solvated with an orthorhombic box of simple point charge water molecules using the Desmond package in Maestro (Desmond Molecular Dynamics System, version 4.6, D. E. Shaw Research).

To generate the molecular dynamics atomic trajectory, the standard system relaxation protocol provided in Maestro was used, followed by 100 ns of NPT molecular dynamics (300 K, 1.01325 bar), during which atomic positions were recorded every 50 ps. To maintain the pressure and temperature of the system, isotropic position scaling and the Nosè–Hoover chain thermostat methods were used with relaxation times of 2 ps and 1 ps, respectively. A RESPA integrator scheme was employed (step: 2.0 fs for bonded interactions; 2 fs for van der Waals and short-range electrostatic interactions; 6 fs for long-range electrostatic interactions). Short-range electrostatic interactions were cut off at 9.0 Å.

For the ensemble docking procedure all non-protein atoms were removed from the 5,000 molecular dynamics frames and the spastin structures from each frame were aligned to remove translational and rotational movement of the macromolecule. One hundred representative frames were selected using the molecular dynamics-trajectory clustering methods in Schrödinger, based on the coordinates of the nucleotide-binding site residues. To remove overlap of the atoms' van der Waals radii, representative structures were minimized using 25 iterations of the Polak–Ribière conjugated gradient method or until the root mean square of the gradient of the energies was <0.05 kJ mol$^{-1}$ Å$^{-1}$, using OPLS2003e force field and a cut-off of 20 Å for the electrostatic interactions and 8 Å for the van der Waals interactions. Molecular docking was performed on the resulting 100 structures using the XGlide script with the OPLS2003e force field and Schrödinger's GlideScore multi-ligand scoring function[47]. A box of 22 Å was placed, centered approximately at the P-loop residues of Dm-spastin. Grids for docking calculations were obtained with the grid generation module in Schrödinger. A scaling factor of 0.8 was applied to the atom radii for every atom with assigned partial charge <0.25. The AROMATIC_H-BONDS option was set true. The major tautomer at pH 7.0 of compound **4** [1-methyl-4-(4-((5-phenyl-1*H*-pyrazol-3-yl) amino)quinazolin-2-yl)piperazin-1-ium] was calculated using the LigPrep panel in Maestro. For docking, the REWARD_INTRA_HBONDS, SAMPLE_RINGS, HBOND_DONOR_AROMH, FORCEPLANAR, and AROMATIC_H-BONDS options were set true, and a scaling factor of 0.75 was applied to atom radii for every atom with assigned partial charge <0.15. Compound **5** ((*R*)-4-(4-((5-(*tert*-butyl)-1*H*-pyrazol-3-yl)amino)quinazolin-2-yl)-3-methylpiperazin-1-ium) and compound **6** ((*R*)-4-(4-((5-(*tert*-butyl)-1*H*-pyrazol-3-yl)amino)-7*H*-pyrrolo [2,3-*d*]pyrimidin-2-yl)-3-methylpiperazin-1-ium) were docked using an analogous procedure.

**Chemical inhibitors.** Compound syntheses and characterizations are reported in the Supplementary Note.

**Reporting Summary.** Further information on research design is available in the Nature Research Reporting Summary linked to this article.

## Data availability

All data generated or analyzed during this study are included in this published article (and its Supplementary Information files) or are available from the corresponding author on reasonable request.

## References

41. Mancuso, G. & Rugarli, E. I. A cryptic promoter in the first exon of the SPG4 gene directs the synthesis of the 60-kDa spastin isoform. *BMC Biol.* **6**, 31 (2008).
42. Uphoff, C. C. & Drexler, H. G. Detection of mycoplasma contaminations. *Methods Mol. Biol.* **946**, 1–13 (2013).
43. Schindelin, J. et al. Fiji: an open-source platform for biological-image analysis. *Nat. Methods* **9**, 676–682 (2012).
44. Feng, B. Y. & Shoichet, B. K. A detergent-based assay for the detection of promiscuous inhibitors. *Nat. Protoc.* **1**, 550–553 (2006).
45. Ziółkowska, N. E. & Roll-Mecak, A. In vitro microtubule severing assays. *Methods Mol. Biol.* **1046**, 323–334 (2013).
46. Pettersen, E. F. et al. UCSF Chimera—a visualization system for exploratory research and analysis. *J. Comput. Chem.* **25**, 1605–1612 (2004).
47. Friesner, R. A. et al. Extra precision glide: docking and scoring incorporating a model of hydrophobic enclosure for protein-ligand complexes. *J. Med. Chem.* **49**, 6177–6196 (2006).

Corresponding author(s): Tarun M Kapoor, PhD (kapoor@rockefeller.edu)

# Reporting Summary

Nature Research wishes to improve the reproducibility of the work that we publish. This form provides structure for consistency and transparency in reporting. For further information on Nature Research policies, see Authors & Referees and the Editorial Policy Checklist.

## Statistical parameters

When statistical analyses are reported, confirm that the following items are present in the relevant location (e.g. figure legend, table legend, main text, or Methods section).

| n/a | Confirmed | |
|---|---|---|
| ☐ | ☒ | The exact sample size (*n*) for each experimental group/condition, given as a discrete number and unit of measurement |
| ☐ | ☒ | An indication of whether measurements were taken from distinct samples or whether the same sample was measured repeatedly |
| ☐ | ☒ | The statistical test(s) used AND whether they are one- or two-sided<br>*Only common tests should be described solely by name; describe more complex techniques in the Methods section.* |
| ☒ | ☐ | A description of all covariates tested |
| ☒ | ☐ | A description of any assumptions or corrections, such as tests of normality and adjustment for multiple comparisons |
| ☐ | ☒ | A full description of the statistics including central tendency (e.g. means) or other basic estimates (e.g. regression coefficient) AND variation (e.g. standard deviation) or associated estimates of uncertainty (e.g. confidence intervals) |
| ☒ | ☐ | For null hypothesis testing, the test statistic (e.g. *F*, *t*, *r*) with confidence intervals, effect sizes, degrees of freedom and *P* value noted<br>*Give P values as exact values whenever suitable.* |
| ☒ | ☐ | For Bayesian analysis, information on the choice of priors and Markov chain Monte Carlo settings |
| ☒ | ☐ | For hierarchical and complex designs, identification of the appropriate level for tests and full reporting of outcomes |
| ☒ | ☐ | Estimates of effect sizes (e.g. Cohen's *d*, Pearson's *r*), indicating how they were calculated |
| ☐ | ☒ | Clearly defined error bars<br>*State explicitly what error bars represent (e.g. SD, SE, CI)* |

*Our web collection on statistics for biologists may be useful.*

## Software and code

Policy information about availability of computer code

| | |
|---|---|
| Data collection | Schrodinger (release 2016.1), NIS Elements (v5.02, Laboratory Imaging), Biotek Instruments Gen5 (v2.04.11), DSF BioRad CFX96 Precision Melt Analysis, LICOR Odyssey software (v3.0), Resolve 3D softWoRx-Acquire (v6.5.2, Release RC1) |
| Data analysis | Microsoft Excel 2011, Graphpad Prism (v6.0), UCSF Chimera (v1.10.2), FiJi (v2.0.0), |

For manuscripts utilizing custom algorithms or software that are central to the research but not yet described in published literature, software must be made available to editors/reviewers upon request. We strongly encourage code deposition in a community repository (e.g. GitHub). See the Nature Research guidelines for submitting code & software for further information.

## Data

Policy information about availability of data

All manuscripts must include a data availability statement. This statement should provide the following information, where applicable:

- Accession codes, unique identifiers, or web links for publicly available datasets
- A list of figures that have associated raw data
- A description of any restrictions on data availability

The datasets generated during and/or analysed during the current study are available from the corresponding author on reasonable request.

# Field-specific reporting

Please select the best fit for your research. If you are not sure, read the appropriate sections before making your selection.

☒ Life sciences ☐ Behavioural & social sciences ☐ Ecological, evolutionary & environmental sciences

For a reference copy of the document with all sections, see nature.com/authors/policies/ReportingSummary-flat.pdf

# Life sciences study design

All studies must disclose on these points even when the disclosure is negative.

| | |
|---|---|
| Sample size | Sample size was not predetermined. Key experiments were repeated three times, which is according to common practice for other works published in nature chemical biology. Normal distribution was assumed for all the experimental measurements in the figures. |
| Data exclusions | No data exclusion was applied. |
| Replication | For biochemical experiments (ATPase activity inhibition, kinetic parameters measurements and differential scanning fluorimetry), all replicates were successful. For cell-based experiments in figure 5 b-c all replicates were successful. For cell-based experiments in figure 5 e-h replicates were not attempted when the level of cellular GFP fluorescence was not distinguishable from background fluorescence using our microscopy setting. For SDS-page gels throughout the paper, replicates were not attempted. Most proteins purifications were independently repeated with similar results. |
| Randomization | No data randomization was performed. |
| Blinding | No blinding was applied. |

# Reporting for specific materials, systems and methods

## Materials & experimental systems

| n/a | Involved in the study |
|---|---|
| ☒ | ☐ Unique biological materials |
| ☐ | ☒ Antibodies |
| ☐ | ☒ Eukaryotic cell lines |
| ☒ | ☐ Palaeontology |
| ☒ | ☐ Animals and other organisms |
| ☒ | ☐ Human research participants |

## Methods

| n/a | Involved in the study |
|---|---|
| ☒ | ☐ ChIP-seq |
| ☒ | ☐ Flow cytometry |
| ☒ | ☐ MRI-based neuroimaging |

## Antibodies

| | |
|---|---|
| Antibodies used | anti-tubulin DM1a, SIGMA cat#F2168-; anti-spastin Sp6C6 Abcam; anti-acetylated tubulin Sigma cat#T7451 |
| Validation | Sigma cat#F2168 validation:<br>1- The Journal of biological chemistry 2007-10-30<br>Takaki et al. Dec 21;282(51):37285-92. Epub 2007 Oct 27.<br>Heat shock transcription factor 1 is required for maintenance of ciliary beating in mice.<br><br>2-Nat Cell Biol. 2011 Aug 28;13(10):1265-71. doi: 10.1038/ncb2327.<br>Formation of stable attachments between kinetochores and microtubules depends on the B56-PP2A phosphatase.<br>Foley EA1, Maldonado M, Kapoor TM.<br><br>anti-spastin Sp6C6 Abcam validation:<br>Hum Mol Genet. 2014 May 15;23(10):2527-41. doi: 10.1093/hmg/ddt644. Epub 2013 Dec 30.<br>Gene dosage-dependent rescue of HSP neurite defects in SPG4 patients' neurons.<br>Havlicek et al.<br><br>anti-acetylated tubulin Sigma cat#T7451:<br>J Cell Biol. 1987 Feb;104(2):289-302.<br>Microtubules containing acetylated alpha-tubulin in mammalian cells in culture.<br>Piperno et al. |

## Eukaryotic cell lines

Policy information about cell lines

| | |
|---|---|
| Cell line source(s) | HeLa-WT and HeLa -N386C cells were derived from the T-REx™-HeLa Cell Line (ThermoFisher cat #R71407). |
| Authentication | This commercial cell line was no authenticated. |
| Mycoplasma contamination | Cell line tested negative for mycoplasma contamination. See Methods for details. |
| Commonly misidentified lines (See ICLAC register) | HeLa from invitrogen were used. These cell line have a genomic FLIP-in site that enable rapid selection of transformants in parallel experiments and allows more direct comparisons to be established between the different transformants |